© 2017 Janet Yue Hung Sheung

OPTICAL INSTRUMENTS FOR CHARACTERIZATION IN THE NANO-SCALE

BY

JANET YUE HUNG SHEUNG

DISSERTATION

Submitted in partial fulfillment of the requirements
for the degree of Doctor of Philosophy in Physics
in the Graduate College of the
University of Illinois at Urbana-Champaign, 2017

Urbana, Illinois

Doctoral Committee:

Associate Professor Yann R. Chemla, Chair
Professor Paul R. Selvin, Director of Research
Professor Nigel Goldenfeld
Professor Brian DeMarco

ABSTRACT

Optical (light-based) instruments are often some of the most precise in many fields, owing to the wide availability of stable and low bandwidth lasers such as those of HeNe and single mode solid state types. Rulers of nanoscale precision and accuracy can be built with such lasers as light sources. This thesis two such instruments, the Florescence Correlation Spectroscope for determination of hydrodynamic size of quantum dot bioprobes to nanometer precision in part one, and the Long Trace Profiler/Optical Slope Measurement System for characterization of line spacing errors in X-ray blazed synchrotron diffraction gratings to the Angstrom scale in part two.

Quantum dots have long been a reliable label in single-molecule applications due to their brightness and photo-stability. These desirable traits come at a price of a large hydrodynamic size, often exceeding that of the protein to be labeled and thus perturbing the biological system under study from its natural state. In size-sensitive applications researchers have used quantum dot probes with less robust encapsulations, and this loss of robustness present challenges for size characterization using traditional chromatography techniques. We discuss the use of fluorescence correlation spectroscopy (FCS) in these situations and report the hydrodynamic diameters, measured by FCS, of quantum dots we have previously successfully employed in the study of a spatially-confined cellular process where both smallness of reporter and brightness to achieve nanometer-scale resolution were necessary. We report that for four colors spanning the visible spectrum our quantum dot probes, both carboxylate and functionalized with streptavidin, are smaller than commercially available counterparts. In particular, our altered amphiphilic ligand coating resulted in a decrease in hydrodynamic diameter of 2.3nm - 4.8nm.

The Optical Slope Measurement System Argonne National Laboratory's Advanced Photon Source (APS-OSMS) is capable of resolving slope errors in

X-ray mirrors down to 50 nanoradian. Now the Department of Energy Synchrotron facilities (Advanced Light Source at Lawrence Berkeley National Lab, National Synchrotron Light Source II at Brookhaven National Lab, along with Argonne APS) need the capability to characterize X-ray diffraction gratings developed in-house, with the APS-OSMS best positioned to receive the necessary additional optics. The development of the hardware additions are discussed, along with successful test scans. Metrology work for three of Brookhaven Lab's newest diffraction gratings are already planned on this newly expanded instrument.

To my teachers and mentors.

ACKNOWLEDGMENTS

This thesis is the culmination of a long and at times arduous course of study. Through this process I have experienced kindness from many people, often unexpectedly.

First, I must acknowledge my advisor Paul Selvin for his guidance and for providing an environment of abundance in which I rarely lacked for resources. Also my thanks goes out to all Selvin labmates past and present with whom I overlapped during this journey. In particular, I learned a lot from Hannah DeBerg, Kevin Teng, Ben Blehm, and Sang Hak Lee. Part of the work in this thesis would not be possible without the team at Inprentus Inc. I am grateful to Peter Abbamonte for his emotional support, inspiration, and offer of opportunities. Also to Jonathan Manton and Lance Cooper for intellectual and emotional support.

The team at Argonne National Lab Advanced Photon Source – Lahsen Assoufid, Jun Qian, Sunil Bean, and Joe Sullivan – have been tremendously supportive and helpful. I have benefitted from the National Lab system since my high school days, having spent two summers as a high school student and the summer between undergrad and grad at Lawrence Berkeley Labs, before my current project at Argonne. My sincerest thanks to the National Lab system not only for what it had done for me personally, but also for all the fantastic outreach and education efforts happening at every lab.

In addition I thank my friends Raymond Clay, Duncan Nall, Yang Bai, Mason Porter, Ted Corcovilos, Ivan Teo, Sukrit Suksombat, Wathid Assawasunthonnet, Ward Lopes, Mike Woods, Zeb Rocklin, and my cat Coonfucius for their company along the way. Thank you to Sharlene Denos, Peter Hung, and Jon Scott with for their help and shared memories from our outreach work. I thank the many students I had the pleasure to teach, in particular many students of PHY402 whose intellectual curiosity and hard work spurred me to become a better educator.

Through my graduate studies I have been generously supported by funding from many organizations. The National Science Foundation through research grants and also through the Center for the Physics of Living Cells, through which I was able to participate in some of the local K-12 Outreach initiatives. I am extremely grateful to the University of Illinois Physics Department for years of support through various teaching assistantships. My deepest gratitude to Inprentus Inc., which supported me through the year where nearly all of the work described in this thesis was conducted. Also I thank the Engineering College's SURGE program for a fellowship appointment and the Marine Biology Lab for financial aid to attend their summer course.

Looking further back in my life, I must acknowledge the influence and encouragement of several teachers and mentors: my high school physics teacher Mr. Robinson who secured went far out of his way to secure an internship opportunity for his student at the local National Lab; my mentors Dr. Bob Cahn who showed me by example what a scientist is, and Dr. Rollie Otto for the many pieces of advice he had given me over more than a decade; my math teacher Mr. Hasson, against whom I still occasionally measure myself as a teacher.

There are many more not listed above, thank you to them too.

TABLE OF CONTENTS

LIST OF ABBREVIATIONS **ix**

I HYDRODYNAMIC SIZE MEASUREMENTS OF QUANTUM DOTS BY FLUORESCENCE CORRELATION SPECTROSCOPY **1**

CHAPTER 1 INTRODUCTION **2**
1.1 A Brief History of Microscopy 2
1.2 Size Scales of Single Molecule Microscopy 5
1.3 The Quantum Dot 5
1.4 Techniques to Measure Nanoparticle Sizes 7
1.5 Summary 10

CHAPTER 2 THEORETICAL BASIS OF FLUORESCENCE CORRELATION SPECTROSCOPY **11**
2.1 The Correlation Function 11
2.2 Data Analysis 12
2.3 Additional Considerations for Quantum Dots 16

CHAPTER 3 THE FCS INSTRUMENT **17**
3.1 Hardware Components 17
3.2 Procedures 23
3.3 Troubleshooting 28

CHAPTER 4 MATERIALS AND METHODS **31**
4.1 Quantum Dot Ligand Exchange 31
4.2 Buffers 31
4.3 Dyes and Commercial Quantum Dots 33
4.4 Sample Chamber 35
4.5 Troubleshooting 35

CHAPTER 5 RESULTS AND DISCUSSION **37**
5.1 DLS Tests 37
5.2 FCS Controls 38

5.3 Laser Power Dependence vs. Core Composition 42
5.4 Effect of Modified Coating on Particle Size 43
5.5 Calculation of Number of Streptavidin per QD 52
5.6 Summary 52

II CHARACTERIZATION OF DIFFRACTION GRATINGS WITH THE LONG TRACE PROFILER 54

CHAPTER 6 INTRODUCTION 55
6.1 Synchrotron Optics, Specifically Diffraction Gratings 55
6.2 The Textbook Diffraction Grating 56
6.3 The VLS Diffraction Grating 58
6.4 The Imperfections Textbooks Do Not Describe 59

CHAPTER 7 EXISTING METROLOGY INSTRUMENTS 64
7.1 Diffractometer 64
7.2 The Littrow Condition 66
7.3 The Long Trace Profiler 66

CHAPTER 8 DEVELOPMENT OF THE APS-OSMS FOR METROLOGY ON VLS DIFFRACTION GRATINGS 70
8.1 Adding Needed Degrees of Freedom 70
8.2 Scan Step-size Comparison 76
8.3 Improved Angle Calibration Using Piezo Rotation Stage 77
8.4 Characterization of VLS Coefficients of IEX Beamline Diffraction Grating 78
8.5 Conclusion and Future Work 81

APPENDIX A APPENDIX – MATLAB CODE 87

REFERENCES 96

LIST OF ABBREVIATIONS

FCS	Fluorescence Correlation Spectroscopy
DLS	Dynamic Light Scattering
bQD	"big", commercially available Quantum Dot
sQD	"small", laboratory made Quantum Dot
VLS	Variable Line Spacing
LTP	Long Trace Profiler
OSMS	Optical Slope Measurement System

Part I

HYDRODYNAMIC SIZE MEASUREMENTS OF QUANTUM DOTS BY FLUORESCENCE CORRELATION SPECTROSCOPY

CHAPTER 1

INTRODUCTION

The aim of the research effort described in part one of this thesis is to accurately determine the size of a specific class of fluorescent bioprobe, the functionalized and size-minimized quantum dot. It was found that an established technique, Fluorescence Correlation Spectroscopy (FCS), could be used to this effect with a few extra experimental controls. This chapter covers background information such as why quantum dots are worth the extra effort to characterize, and other available techniques for measurement of particle size, in order to provide context to the reader. It may be skipped in its entirety in favor of getting immediately to the specifics (FCS in chapter 2, ampiphilic ligand coated CdSe quantum dots in chapter 3).

1.1 A Brief History of Microscopy

Through the course of centuries our ability to visualize biological processes on the molecular scale had evolved from first being limited by the quality of available optics, then by the diffraction limit of the light forming the images, to finally being limited by the number of photons detected [1]. Arguably the first microscope was that used by the 17th century Dutch scientist Antoine von Leeuwenhoek. It consisted of little more than a small glass sphere like those formed by melting glass rod or capillary, and with it he made the first recorded observations of micro-organisms including bacteria.

The first microscope with all the same parts as a modern student grade microscope was invented by Robert Hooke, as seen in the left side of Figure 1.1. None of the lenses had any aberration correction, and in fact the large lens which functioned as the condenser was a spherical glass tank filled with water instead of solid glass, but it was already powerful enough to observe the dried plant cells in a piece of cork.

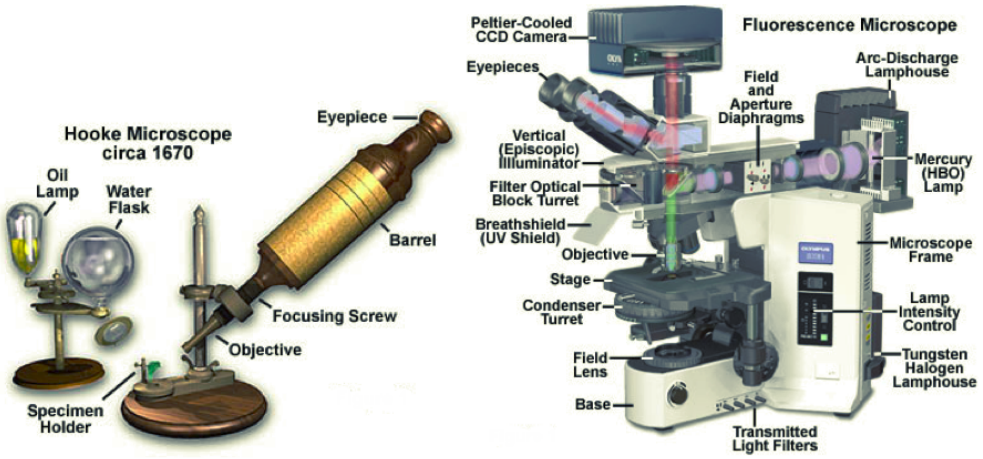

Figure 1.1: Left: Seventeenth century microscope as used by Hooke when he coined the term cell. Primitive versions of not only the eyepiece, objective, and lamp, but also condenser (water flask) could be seen. Right: Typical modern research grade fluorescence microscope commonly found in biology labs. Images courtesy of Olympus Microscopy Resource Center.

As the craft of lensmaking became perfected, for example through combining multiple lenses as in doublets and triplets or by refining the surface curvature as in aspheres to correct for aberrations, eventually the performance of microscopes reached the Abbe limit as given by

$$\mathrm{d} = \frac{\lambda}{nsin(\theta)}$$

where d denotes the diameter of the formed image of an ideal point source of light, λ the wavelength of light, n the index of refraction, and θ the half angle of the light cone collected by the objective [2]. Current state of the art objectives place the upper limit of n at 1.6 (high n). Then using green light as representative of the middle of the visible spectrum ($\lambda \sim 550$ nm) and knowing the maximum of the sine function is 1, we derive a spot width of 344 nm. This is the limit imposed by the wave nature of light: all objects smaller than this will still appear this size as seen through the microscope. This is more than a minor inconvenience considering that one of the most popular model organisms in biology, E. Coli, has typical dimensions 1000x3000 nm (1x3μm), which is not much bigger than this limit.

It was known from diffraction theory that this spot, called the point-spread

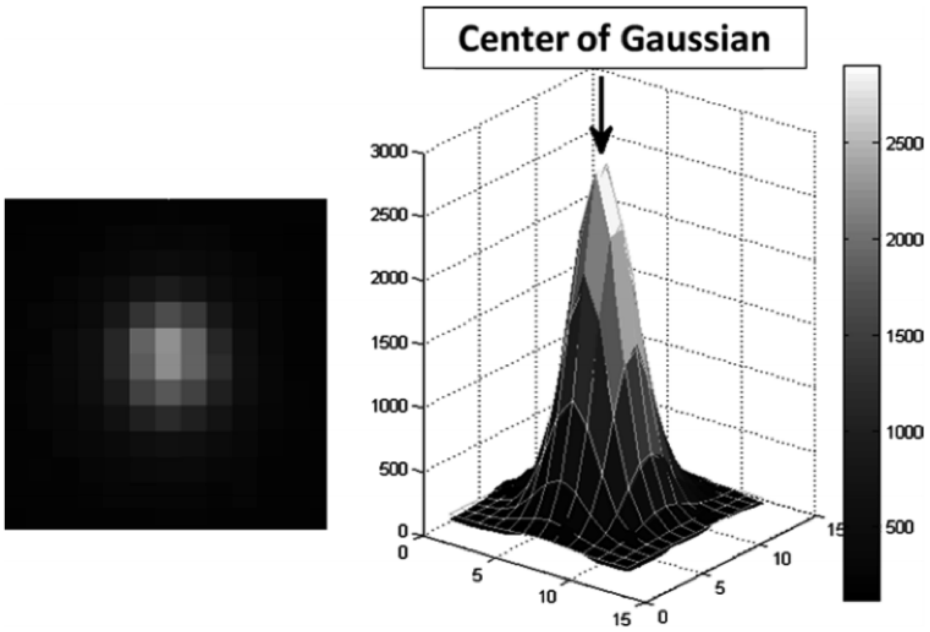

Figure 1.2: Computer post-processing can enhance the resolution of a microscope by two orders of magnitude. Here, the camera captured point spread function of a fluorescent label is fitted to a three-dimensional Gaussian to locate the central peak. (Figure as published in book chapter co-written with Melinda Hoffman [6].)

function, has a specific functional form ($sinc^2$) with a prominent central peak which could be localized within the width of the spot itself [3]. However it was not until cameras became digital and computers were powerful enough to read and process images quickly that such post-processing became commonplace. Many methods exist to localize the peak, with the trade-off being computation time versus precision. When speed is desired a popular option is to simply compute the centroid of the intensity distribution as the point-spread function should be symmetric; when high precision is paramount the peak is often found by fitting the intensity distribution to the three-dimensional Gaussian as shown in Figure 1.2) [1]. Different estimates of where this puts the resolution limit exist, with general concensus around one nanometer [4, 5]. With this, the world of molecular biology opened to the visible light microscope.

In parallel with this development other optical components in a microscope also improved significantly in quality. Of particular note, mastery of thin film deposition techniques made possible for optical filters to be manufac-

tured with transmission spectra customized to pass and block distinct color channels. Judicious selection of such filters to match the emissions of available fluorophores allows an optical system to separate the signals to different recording devices, for example a camera. At the current state of technology the number of channels achievable is limited only by funds and engineering prowess, though before that point one can expect to run into issues with SNR (due to loss in efficiency from the complex optical path) and availability of fluorophores which the sample could be labeled with at once. Results with five, even six channels have been published in high profile journals (cite multi color). In this way, all participants in a complex, multi-protein interaction could be monitored simultaneously and co-localized.

Nanometer-precision fluorescence microscopy images have furthered understanding across a wide variety of disciplines in biophysics, in vitro and in vivo, for over a decade. Using organic dyes localization to nanometers was achieved at sub-second time resolution, and subnanometer resolution was demonstrated at a lower time resolution of multiple seconds [5, 7, 8]. Localizing many individual particles over multiple frames is the basis for state-of-the-art super-resolution techniques [9, 10].

1.2 Size Scales of Single Molecule Microscopy

Though molecular probes made of fluorophores open up a wealth of possibility in terms of what could be studied, there are important practical considerations regarding their use. One such question is: To what extent does the introduction of these probes into the system perturb the system? It turns out that often the labels could be similar in size to the protein to be labeled, such that the final probe-protein complex becomes significantly different in size and shape from before.

1.3 The Quantum Dot

Much progress has been made on improved probes such as engineered dyes with increased lifetimes and various strongly scattering or fluorescent nanocrystals [11, 12, 13]. In particular, quantum dots have been embraced for their

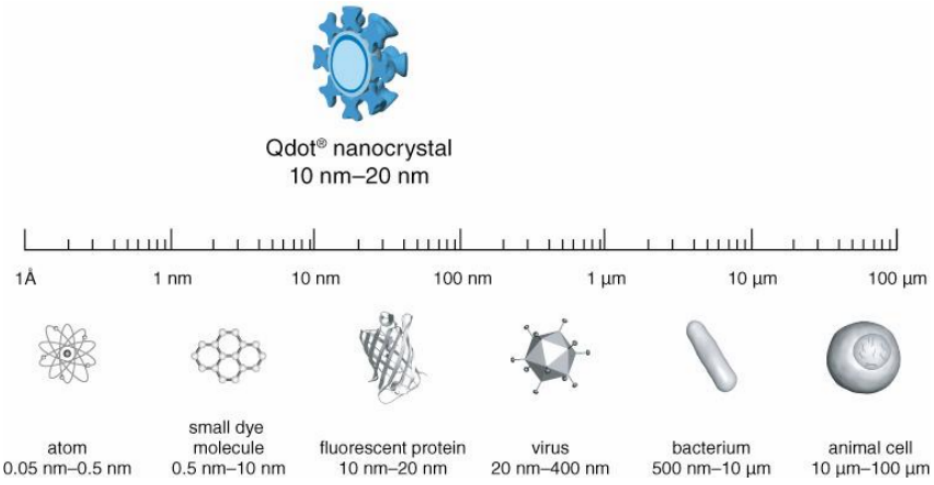

Figure 1.3: The size of quantum dots, a popular fluorophore, relative to various size scales of biological interest. (Figure courtesy of Invitrogen)

exceptional fluorescence which is size-tunable to peak anywhere on the visible spectrum [14, 15, 16]. With complex biological systems increasing demands on the number of distinct color channels to be imaged in parallel, quantum dots are quickly becoming an indisposable tool.

The fluorescence of a quantum dot originates from a core, typically of Cadmium Selenide (CdSe) or Cadmium Selenide Telluride (CdSeTe), enhanced by a thin coating of Zinc Sulfide (ZnS). This hydrophobic particle then requires at least one additional coating to become soluble in water and therefore biocompatible. Any functionalization for desired specific targeting further increases the size of the completed probe.

A survey across different coating strategies by Smith et. al. concluded that while encapsulation by amphiphilic polymers can yield high chemical stability, it comes at a cost of significantly increased hydrodynamic size compared to encapsulation by a monolayer of a hydrophilic ligand [17]. Commercially available water solubilized quantum dots are universally polymer-coated, as the stability of the probe is generally important whereas the effect of a size difference of a few nanometers depends entirely on the intended application. However at around 20nm in diameter commercial functionalized quantum dots are often comparable in size to their labeling targets, and in 2014 our lab observed quantifiable differences in the diffusive behavior of neuronal receptors labeled with commercial quantum dots versus those with a min-

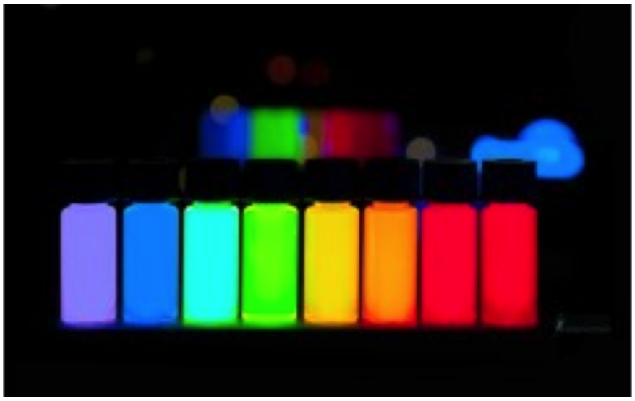

Figure 1.4: Some examples of colors of quantum dots commercially available. Image from: http://www.plasmachem.com/shop/en/226-zncdses-alloyed-quantum-dots

imal ligand coating [18]. Though this study was conducted in a specific biological system, the presence of narrow passageways inaccessible to a large protein-probe complex can be expected in a wide variety of cellular imaging applications [19]. In these situations it is important to characterize the hydrodynamic size of the probes well, and, keeping in mind the reduced stability of quantum dots with the ligand coating, to do so without causing damage to the probe.

1.4 Techniques to Measure Nanoparticle Sizes

Multiple established techniques exist for determination of hydrodynamic size of fluorescent probes.

1.4.1 Transmission Electron Microscopy

In Transmission Electron Microscopes (TEM) an electron beam takes the place of the light beam in optical (light) microscopes. Due to the significantly shorter wavelengths achievable with an electron beam, some 100,000x less than that for a visible light beam (λ_e = 6pm versus λ_L = 600nm), TEMs can resolve down to individual atoms with no difficulty. However, in this technique it is how much the electrons are scattered versus transmitted which sets the contrast in the image formed. While the metallic cores of quantum

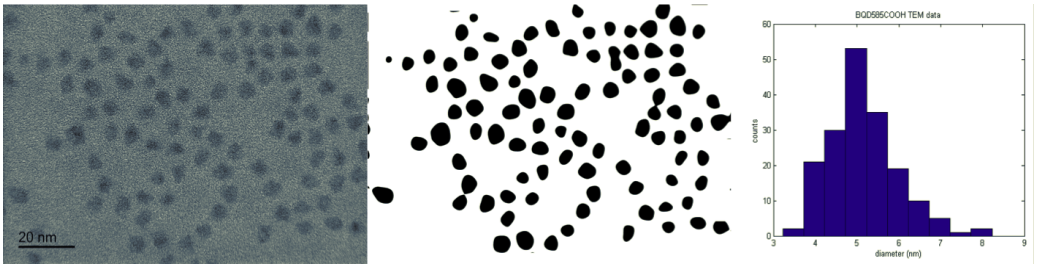

Figure 1.5: Left: Example of TEM micrograph of some quantum dots, showing the CdSe core. Middle: Intensity threshold applied to find the edges for determining size. Right: Histogram of diameter measurements from this dataset. Micrograph courtesy of Sung Jun Lim.

dots exhibit strong scatter and therefore stand out in high contrast from the background in a TEM image, any ligand coating and functional groups do not, and so are invisible under TEM.

This is one reason why there is little debate about the sizes of the quantum dot cores, while the size of the full fluorescent bioprobe remains an open question.

1.4.2 Chromatography

High-performance liquid chromatography (HPLC) and low pressure variants of size exclusion chromatography such as gel filtration chromatography (GFC) separates the constituents of a sample by size via retention time through a column, allowing accurate measurement through comparison against well-calibrated standards without need for complicated analysis involving various assumptions [20, 21].

The manufacturer of some of the quantum dot core/shells used in this study, Thermofisher Scientific, informed us through private communication that HPLC is their technique of choice for internal quality control. However our completed probes with the quantum dot core/shell surrounded only by a minimal hydrophilic ligand coating lacked the robustness to travel through the column intact, leading not only to loss of sample but occasionally even necessitating costly replacement of the column itself. As this decrease in robustness is a necessary trade-off to minimizing size, we turned to non-contact techniques less demanding on the sample while still providing comparable accuracy.

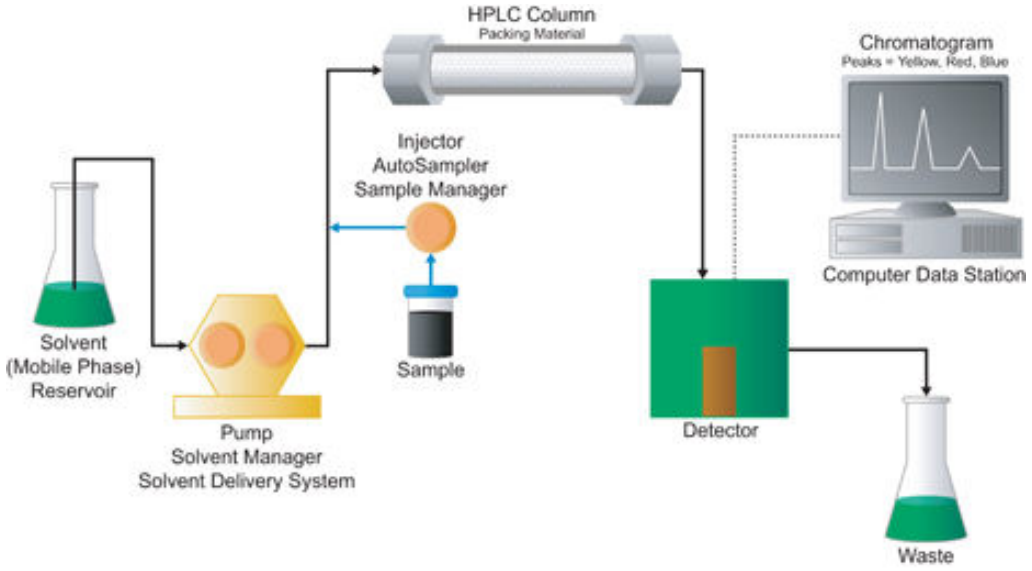

Figure 1.6: Simplified diagram of a typical HPLC system, showing the injection pathway and separating column. Image courtesy of Waters Corporation.

1.4.3 Dynamic Light Scattering

One such technique, dynamic light scattering (DLS), requires only that the particles scatter an incident beam for a measurement of their mean particle size. It is also conveniently available within the form factor of a benchtop instrument, for example the Malvern Zetasizer used in this study. The scattered light is collected and its fluctuations taken to reflect the Brownian motion of all particles, which then allows hydrodynamic size to be derived via scattering theory [22]. Different assumptions could be made during the analysis yielding different derived size distribution from a single dataset, and modern DLS instruments automate all of these computations down to a few button clicks and input of the needed parameters [23]. However these parameters are material-dependent and not well-known for quantum dots. Published literature provide examples of DLS-measured quantum dot size being reported from different distributions, listed by increasing complication of analysis – intensity distribution [24], volume/mass-distribution [15, 19], and number distribution [25, 26, 27]. As volume goes as $diameter^3$ and scatter intensity goes as $diameter^6$, these distributions are skewed by even a small degree of polydispersity. On the other hand, as the derivation of the number distribution requires the most additional parameters and computational steps, it is the least reproducible and its accuracy most difficult to estimate. When the

sample is monodisperse the different estimates should closely resemble each other, for example as reported in Susumu et. al [28], but a spread of more than one nanometer is to be expected. Thus despite the convenience of the technique, the output requires considerable expertise to interpret if precision beyond this is desired. Furthermore, the theoretical basis of this technique relies on scatter being the only source of signal, and this assumption is false for quantum dots which exhibit high absorption and strong fluorescence. All these effects are coupled into the signal collected by the instrument and contribute to error the magnitude of which depend on the quantum yield, absorption cross-section and scattering cross-section of the particular sample, all functions of wavelength. Though this error can be minimized by inserting an optical narrow filter, its magnitude is difficult to estimate even when the exact fluorescence spectrum of the quantum dot is known. Commercial DLS systems often use a red light source, and though such systems work very well in cases where emission wavelength under 580nm, their size measurements are difficult to interpret for the red emission quantum dots. Unfortunately quantum dots emitting in this portion of the spectrum tend to be the brightest and are used often especially in multicolor imaging, where fluorophores must be chosen to be spectrally distinct to avoid channel cross-talk.

1.5 Summary

The aim of this part is to present FCS as a good alternative for size measurement where accuracy is desired, especially when size exclusion chromatography is unavailable or could not be used. Also, we report the hydrodynamic sizes of quantum dots coated with a layer of C11-(PEG)4- ligand (schematic shown later in Figure 4.1) instead of the customary polymer coating, and demonstrate that both across the emission spectrum, and with or without streptavidin-functionalization, our quantum dots are smaller than those commercially available.

CHAPTER 2

THEORETICAL BASIS OF FLUORESCENCE CORRELATION SPECTROSCOPY

2.1 The Correlation Function

Fluorescence fluctuation spectroscopy (FCS) is similar to DLS in principle and analysis, but using the fluorescence emission and not scattered light as raw signal. The fluorescence signal can be effectively isolated from the excitation and any scatter with the same dichroic and/or optical filter which will be needed in the microscope when using the quantum dot as a fluorescent probe. The wide absorption spectra of quantum dots means equipping the FCS with a single laser, at a blue or near ultraviolet wavelength, is sufficient to excite all color quantum dots in the visible spectrum. Relative to DLS, FCS will also diagnose common issues specifically relevant to the quantum dot's performance as a biological probe, for example unusually low fluorescent signal due to core/shell damage or high non-specific binding are readily seen.

Much literature exists on FCS beyond the description to follow [29, 30, 31, 32], and the reader may refer to them for derivations and further detail. In brief, the self-similarity of the fluorescent signal $F(t)$ as a function of time delay τ_D, defined as:

$$G(\tau) = \frac{\langle \delta F(t) \cdot \delta F(t+\tau) \rangle}{\langle F(t) \rangle^2} \tag{2.1}$$

is a monotonically decreasing function in τ with drops at any time constants inherent in the signal, one of which corresponds to the average time required for a particle to diffuse across the excitation focal volume, τ_D. Assuming the focal volume to take the shape of a three-dimensional Gaussian, $G(\tau)$ is well fit by the expression:

$$G(\tau) = \frac{1}{\langle N \rangle} \cdot \frac{1}{1 + \frac{\tau}{\tau_D}} \cdot \frac{1}{\sqrt{1 + (\frac{r_0}{z_0})^2 \cdot \frac{\tau}{\tau_D}}} \tag{2.2}$$

where $\langle N \rangle$ denotes the average number of particles in focal volume, and r_0 and z_0 describe the lateral and axial width of the focal volume respectively. r_0 and z_0 must be determined by the exact optics and calibrated for each system. The diffusion coefficient D can be determined from the diffusion time constant τ_D by:

$$\tau_D = \frac{r_0^2}{4 \cdot D} \tag{2.3}$$

from which the Stokes-Einstein equation is then used to derive the hydrodynamic radius r_h assuming the particle is a sphere:

$$D = \frac{k_B T}{6\pi\eta r_h} \tag{2.4}$$

Organic dyes for which diffusion coefficients well determined by other techniques such as NMR [33], are used for calibration. Due to the presence of triplet state $G(\tau)$ must be fit with an extra term containing τ_T, the time constant of the triplet state:

$$G(\tau) = (1 - T + T \cdot e^{\frac{\tau}{\tau_T}}) \cdot \frac{1}{\langle N \rangle} \cdot \frac{1}{1 + \frac{\tau}{\tau_D}} \cdot \frac{1}{\sqrt{1 + (\frac{r_0}{z_0})^2 \cdot \frac{\tau}{\tau_D}}} \tag{2.5}$$

In a well-aligned system, Angstrom-level size resolution can be achieved [34].

2.2 Data Analysis

Calibrations for our FCS measurements were done with rhodamine 110, using the diffusion coefficient $4.4x1010m^2s^{-}1$ as reported by Gendron et. al corrected for temperature [33]. Throughout the course of experiments the instrument was calibrated daily, with the results shown in Figure 2.4 being representative. Similarly, an example correlation curve for a quantum dot is shown in Figure 2.3.

Typical focal width of the instrument is $\sim 200nm$.

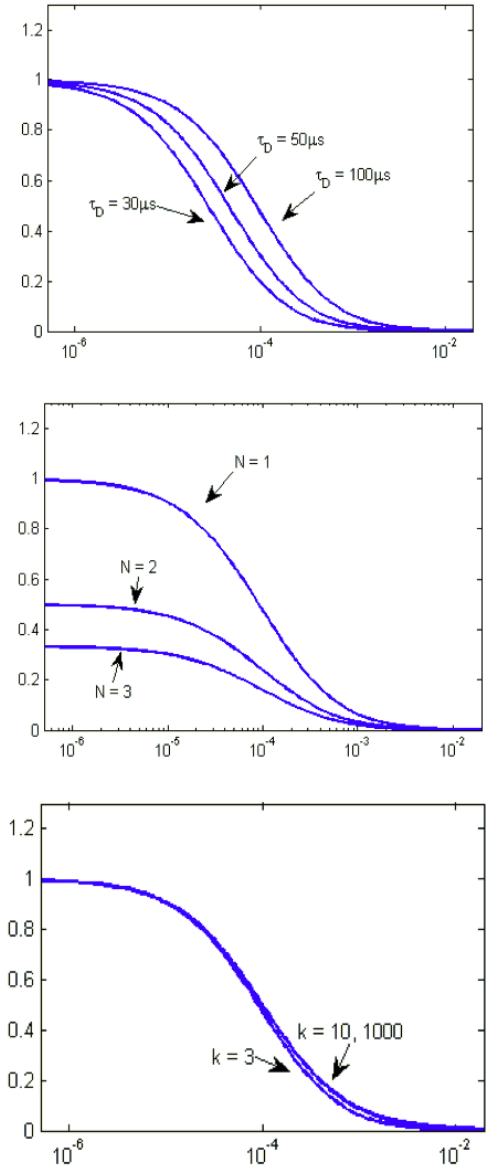

Figure 2.1: Top: A longer average transit time per particle through the focal volume corresponds to a later drop-off in the correlation $G(\tau)$. Example curves are of typical values of τ_D. Middle: The average number of particles in the focal volume per unit of time, N, determines the y-intercept $G(\tau = 0)$. Bottom: The variable k, a measure of the aspect ratio of the focal volume, has a relatively minor effect on the shape of $G(\tau)$, as seen here where k of 10 versus $10,000$ is barely distinguishable.

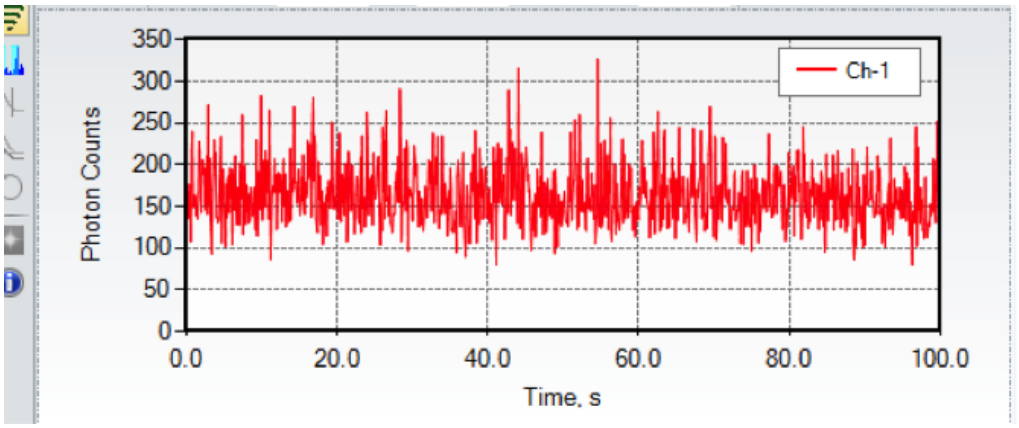

Figure 2.2: An example of the raw intensity time trace recorded by the avalanche photodiode during a FCS measurement. Typical order of magnitude of photons detected per second is only 100 for the excitation intensities used.

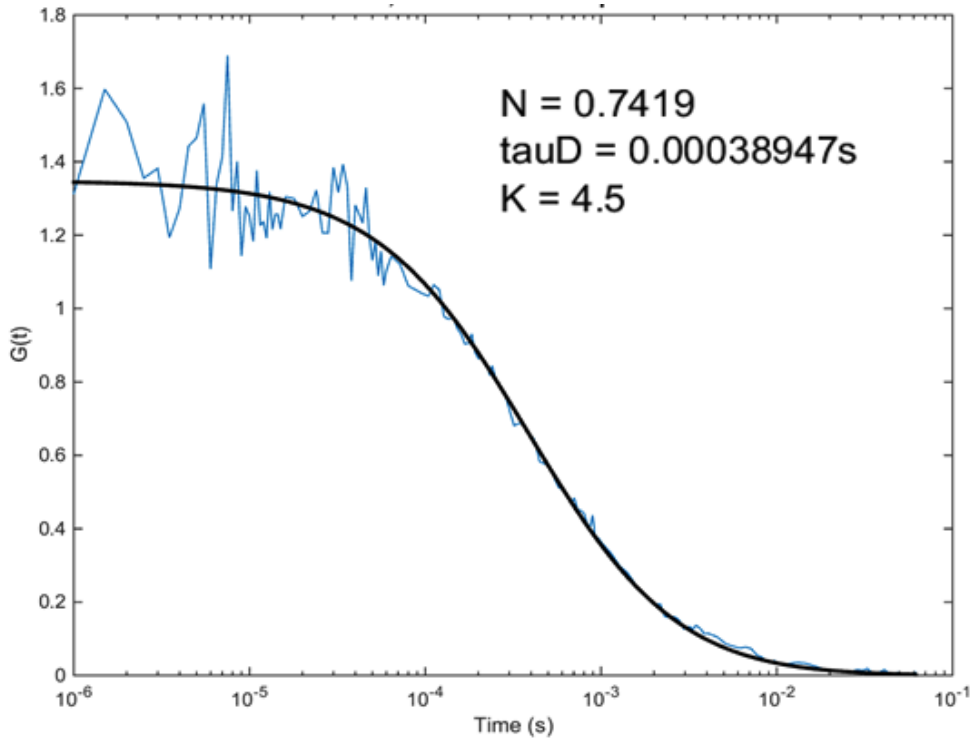

Figure 2.3: Example of a fit for a particle which does not exhibit a triplet state. Note that in this case the correlation function decays all the way to zero in a single drop, at $t = \tau_D$.

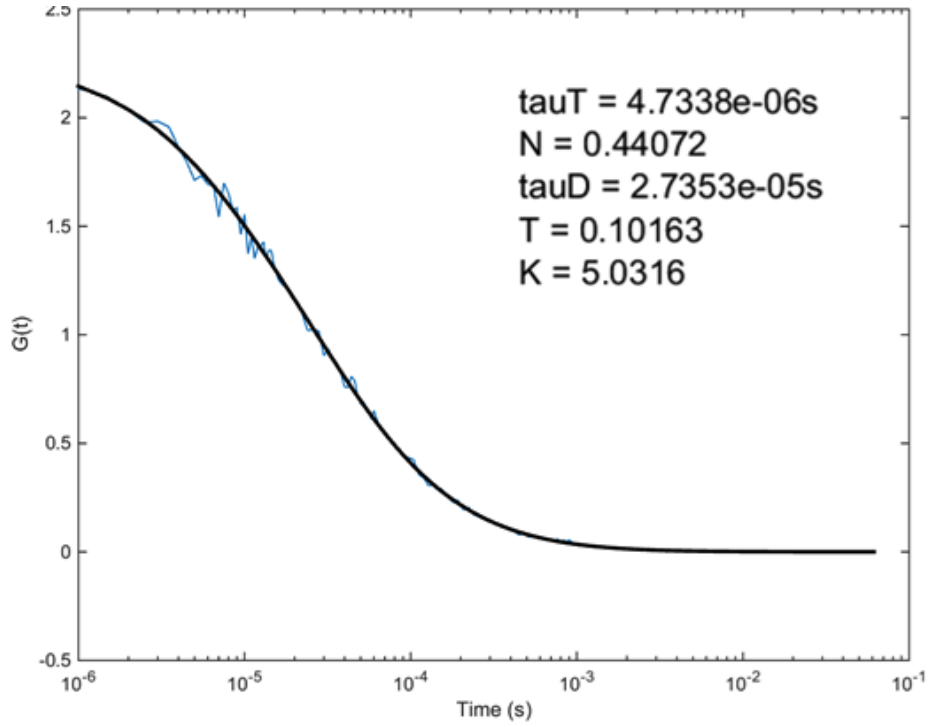

Figure 2.4: Example of a fit for a particle which has a triplet state. In this case the correlation function decays to zero in two drops, at $t = \tau_T$ and $t = \tau_D$.

2.3 Additional Considerations for Quantum Dots

The theory as laid out in section 2.1 for a particle without a triplet state can be applied to the case of quantum dots with only one caveat: the fluorescence of a quantum dot is in general not constant over time for a given excitation intensity, nor is its average value, over the timescale of an FCS measurement, a simple function of the excitation intensity. This violates an implicit assumption used to derive eq. 2.2.

The two known photophysical phenomena contributing to this behavior are blinking – the quantum dot switching into and out of a dark state of significantly diminished intensity at all timescales – and optical saturation, where past a threshold excitation intensity the resulting emission ceases to increase proportionally to further increase in excitation intensity. Careful controls must be done for both phenomena to determine the optimal conditions for size measurements in order to achieve the subnanometer size accuracy we desire. These controls will be discussed later in Section 5.2, and their results will ultimately inform the experimental conditions chosen for the size measurements.

CHAPTER 3

THE FCS INSTRUMENT

This chapter will detail the necessary information for rebuilding and maintaining the FCS instrument as diagrammed in 3.1, including design considerations and troubleshooting steps.

3.1 Hardware Components

3.1.1 The Laser

The first and arguably most important component in an FCS system is the laser. That it emits an ideal TEM_{000} single-mode beam is one of the first assumptions made in the theory laid out in the previous chapter. The focal volume formed by the instrument cannot be reasonably approximated by a three-dimensional Gaussian when the laser is not mode-stable, or is plainly emitting the wrong mode. Its wavelength determines the variety of fluorophores which could be excited and therefore could be measured.

As quantum dots with emission peaks spanning yellow to deep red in color are the particles to be measured in this study, the laser was chosen to be 488nm. This wavelength can excite those quantum dots at efficiency 5%, with the efficiency increasing as the quantum dot shifts towards red (Figure 3.2).

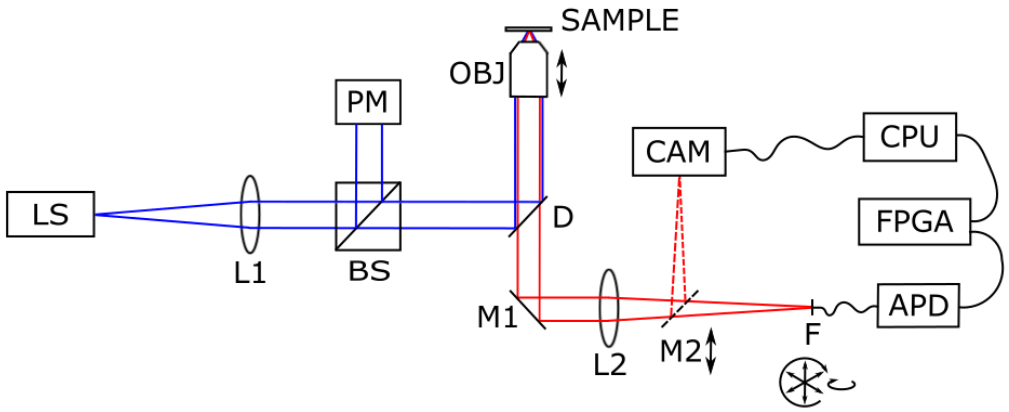

Figure 3.1: Schematic representation of the FCS system, homebuilt around a commercial microscope frame with laser source (LS), beam splitter (BS), dichroic (D), microscope objective (OBJ), camera (CAM) and avalanche photodiode (APD). L denotes lenses and M denotes mirrors.

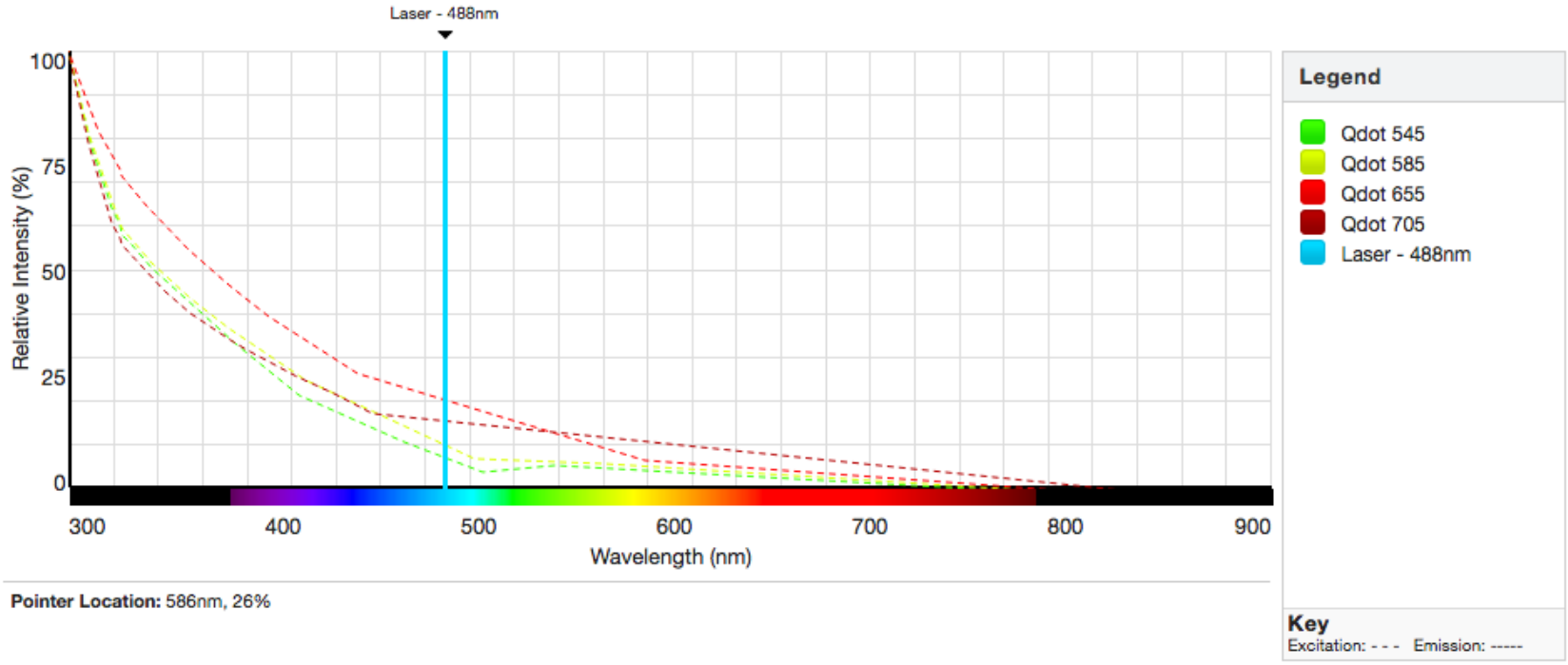

Figure 3.2: Excitation spectra of the quantum dots measured in this project. Plot courtesy of manufacturer, ThermoFisher Scientific.

3.1.2 The Microscope Objective

A high quality beam still requires an objective devoid of significant aberrations to focus into a tight, symmetric volume. Furthermore, the presence of viscosity as a variable in equation 2.4 imply that measurements must be performed sufficiently far away from any surfaces, in particular the glass surface, that surface drag induced viscosity corrections are negligible and the nominal viscosity value for the buffer may be used. The rule-of-thumb is to focus $25\mu m$ above the cover glass.

Practically this requirement rules out the use of oil-immersion objectives as they lack sufficient depth-of-focus, even though for any given excitation wavelength these high index-of-refraction and therefore high numerical aperture objectives focus to the tightest spot size due to the diffraction limit going as $\frac{1}{\lambda}$. Fortunately water immersion objectives can focus to the correct plane, and they are a popular choice for FCS systems.

For the specific instrument used in this study, a 60x magnification, chromatic aberration and flat-field corrected objective is used.

3.1.3 Dichroic

Aside from common sense requirements that it does not distort the beam by being bent or dirty, the dichroic in the optical path serve to set the spectral bandwidths of the excitation and emission paths. In this system, a long-pass dichroic with cut-off at a wavelength of $500nm$ allows all fluorescence emission of wavelength longer than $500nm$ through to the APD equally. This has a direct effect on the final size measurement in the case of quantum dots due to their well-known property of size-tunable emission (Section 1.3). A dichroic which blocks part of the emission distribution then would blind the instrument to certain parts of the size distribution as an unintended consequence. The dichroic made by Semrock used in this study drops sharply from 100% transmission to 0% transmission, so virtually none of the wavelengths transmitted experience attenuation.

3.1.4 Single-Mode Optical Fiber

A pinhole of the order of tens of microns is necessary in the beam path to eliminate poorly-focused stray light. In this system a single mode fiber with core diameter $50\mu m$ functions as the pinhole.

3.1.5 Avalanche Photodiode

The avalanche photodiode (APD) used here is a single-photon counting module (SPCM) with sensitivity on the order of half a photon. Stringent limits on the excitation power as determined by scientific considerations, to be discussed in 5 means that for certain experimental conditions the fluorescence signal is very low. In those cases the quantum efficiency and dark count level of the APD makes the difference between a measurement being possible versus not.

In general the time resolution of an FCS system is set by the APD. When timescales of interest are in the nanosecond regime, for example when studying rotational or vibrational states, electronic noise individual to each photodetector will affect the derived correlation as they are of non-negligible magnitude over these timescales. In these cases the strategy is to divide the signal equally between two APDs, and cross-correlate these to identify the common signal from the individual noise signatures.

Quantum dots peaking in the visible spectrum are of the order ten nanometers in size, corresponding to diffusion times in the tens of microseconds given the other parameters of the instrument. Data analysis for them also do not require a triplet state time constant or other nanosecond timescale constants to be extracted from the data. Therefore it is sufficient to employ a single APD, and simply discard the high frequency data corresponding to timescales shorter than one microsecond. Given the high cost of SPCMs (several thousand dollars) and the increased complexity involved to align and maintain a second detector, this is a significant benefit.

3.1.6 The Field-Programmable Gate Array

The field-programmable gate array (FPGA) functions as a hardware correlator with onboard high precision clock, with enough time resolution to handle

the refresh rate of the APD. In general FPGAs with time resolution down to single nanoseconds are available [35], but since here we are ignoring sub-microsecond timescale completely, the emphasis on the FPGA was its ability to interface with software and its user-friendliness. After initially trying to build around one of the best specced FPGA cards demonstrated to work in an FCS instrument, we went with a hardware and software bundle from ISS.

3.1.7 The Camera

A small camera which can be switched into the beam path by a flip mirror (M2 in figure 3.1). While not directly related to data collection, this camera is necessary to judge depth of focus by giving the operator a means to located the top and bottom glass surfaces of the test chamber. This will be discussed further in the protocol in Subsection 3.2.1.

3.1.8 The rest of the instrument

The rest of the instrument consist of parts to direct the beam between the aforementioned components (mirrors, beamsplitter) and change its collimation (lenses).

An external f = +150mm lens replaces the removed tube lens, and it focuses the signal into the single mode fiber, which is then collected by the SPCM. Autocorrelations were computed using an system (ISS) with each data trace of 100s correlated as ten sections of 10s length, to check for self-consistency. Large spikes (> 3 sigma) in the raw intensity trace and misshapen correlation curves are taken as indications for presence of aggregates and those data were discarded. The filtered autocorrelation curves are then fit using a MATLAB script.

MATLAB scripts used are included in the appendix for completeness.

For easy reference, the exact model of each crucial component is listed in Table 3.1.

Table 3.1: List of Components in FCS Instrument

Component	**Make**	**Model**
Laser Source	Coherent	OBIS488
Aphalanche Photodiode	PerkinElmer	SPCM-AQRH-14-FC
FPGA	ISS	A320 FastFLIM
Microscope frame	Olympus	IX-71
Objective	Olympus	UPlanSApo 60xW/1.20NA
Single mode fiber	Thorlabs	$50\mu m$ core
dichroic	Semrock	500LP
camera	ImagingSource	DMK21BU-04

3.2 Procedures

As designed the FCS system only requires minor tuning each day to achieve best performance. This procedure is described in Subsection 3.2.1. However, due to the sensitivity of alignment of the emitted signal into the optical fiber input of the SPCM, periodic re-alignment is necessary, and for this the full alignment procedure in Subsection 3.2.2 should be referenced.

3.2.1 Measurement

1. Start up system
   (a) Turn on laser power supply sliding switch.
   (b) Wait 30 seconds then turn key-switch to ON position. After a minute the laser should lase and the LASER READY light on the power supply should turn on.
   (c) Power on the ISS FastFLIM box.
   (d) Start Vista software on the dedicated FCS computer by clicking on the desktop icon.
2. Optimize alignment into APD
   (a) Place two drops of immersion water onto 60xW objective and mount concentrated dye sample (concentration $1\mu M$).
   (b) Adjust ND filter in excitation path to ND4.6 (maximum).
   (c) Make sure the flip mirror (M2 in figure 3.1) is down so the light path goes to the APD not the camera.

(d) Start Coherent OBIS software on computer. Type in laser power setting 0.5%.

(e) Set acquisition parameters: acquisition frequency 1kHz (lowest setting), acquisition time 500s.

(f) IMPORTANT: Turn off room light before switching on power strip of the APD.

(g) Press green arrow button on the software screen to start the real-time readout of the APD. Reading should be 150-250 counts; if higher than that check for stray light.

(h) Open the lid of the box around the emission path optics. Reading should still be 150-250 counts. If it is higher make sure it is not due to the computer monitor by blocking it. If it is the monitor, this is a sign that the APD fiber is severely misaligned and potentially a full realignment is necessary.

(i) When dark counts look reasonable, open the laser shutter. If you are using the existing alignment sample the signal level will be somewhere between the dark count value and 21,000 counts per second. IMPORTANT: If counts is above 200,000, shutter the laser immediately to prevent permanent damage to APD.

(j) Stop the real time signal monitor and start the timed acquisition. The time-averaged trace is much easier to read changes from.

(k) Focus the objective upwards by turning the focus knob on the microscope frame. Maximize the signal.

(l) Adjust the x- and y- axis translations on the APD optical fiber. These are the knobs on the fiber mount, translating in the plane PERPENDICULAR to the optic axis. Maximize signal. If the maximum reached is known best value for the test sample (21,000 cps for the pre made one), skip next step.

(m) Adjust the z- axis (along optic axis) translation of the stage under the fiber mount. This degree of freedom is less sensitive so it will need to be turned much faster for an effect to be seen on the cps. Maximize signal, and if necessary, do iteratively with x- and y-translation described in previous step.

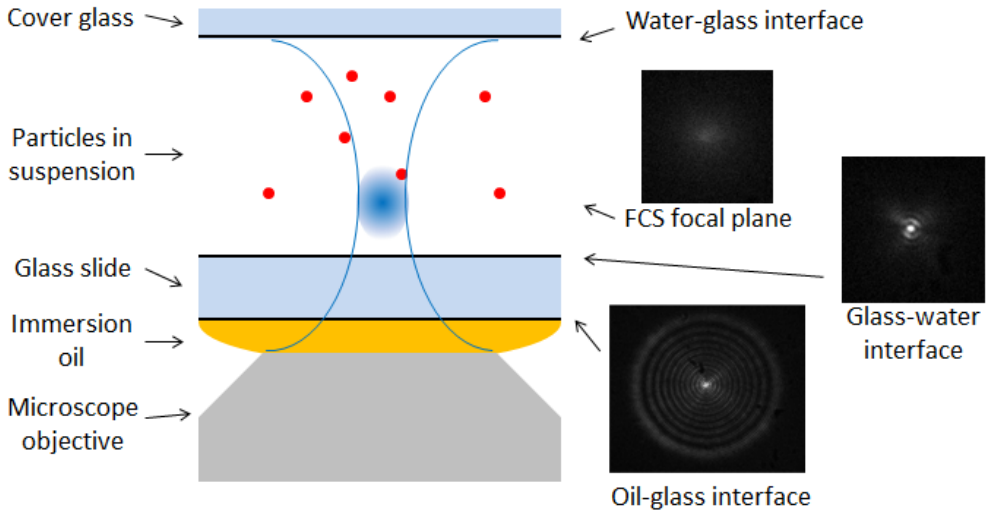

Figure 3.3: Schematic showing the FCS focal volume inside the microfluidic channel, along with what should be seen on camera at various planes when the system is in proper alignment.

(n) Now the APD is aligned and the focal volume shape should be good. Remember to end acquisition and turn off the APD before switching room lights on.

3. Calibrate for focal volume width

(a) Make a sample of rhodamine 110 at $1nM$ concentration diluted in same buffer as the experimental samples. Many other dyes such as rhodamine 6G and Cy3 can and have been used also.

(b) Mount the sample and set attenuation filter to ND1. Flip mirror M2 up to direct emission to camera.

(c) Start camera software IC Capture, then start the acquisition. Focus up and down to locate the three glass-water interfaces where the laser spot could be imaged. These planes are defined in Figure 3.3.

(d) Adjust focus to $25\mu m$ above the top of the cover glass. This is the desired focal plane and you should see a diffuse two-dimensional Gaussian profiled spot on camera.

(e) Stop camera acquisition and flip M2 back down, we don't need to look at the signal on the camera anymore.

(f) Lower attenuation filter to ND3 because you will be using the APD now.

(g) Start Vista software and set acquisition parameters: acquisition frequency 2MHz, acquisition time 100s. Set desired laser power percentage by software.

(h) When everything is ready, turn off room lights and turn on APD.

(i) Acquire at least five data traces. Traces should resemble closely the shape as seen in Figure 2.4 and should be very consistent from trace to trace.

(j) Process traces with Matlab code for empirically determined values of the focal volume parameters w_0 and K; w_0 should be around 200nm and K should not be at either end of the fitting range, at $K = 3$ and $K = 6$.

4. The FCS instrument is now ready to take the real experimental data.

3.2.2 Full Alignment

For clarity all components will be referenced by its label in schematic Figure 3.1.

1. Excitation path

   (a) Check collimation of laser beam from LS. This is set by the distance between the end of the laser pigtail to L1.

   (b) Laser must not clip BS and D. This can be checked by removing OBJ to look at the beam shape being sent into OBJ.

   (c) Laser emerging from OBJ should come to a sharp focus a few millimeters above it.

   (d) Confirm lack of aberrations in the spot by imaging a plain piece of cover glass on CAM. Focus spot should be circularly symmetric as in screenshots in Fig. 3.3. If not, redo the alignment.

   (e) When excitation path alignment looks perfect, proceed to the excitation side.

2. Emission Path (Mostly the APD)

   (a) Illuminate an ultra-bright sample such as an acrylic slide to get a visible beam to align to.

   (b) L2 only needs to be placed so that the emission out of the microscope side port is roughly centered and perpendicular.

   (c) Unscrew optical fiber F from the APD end and point it at a white piece of paper to check whether it is receiving signal. You may need to dim the lights to see it.

   (d) If there is a signal – adjust all five axes on the mount on the other end of the fiber to optimize the signal by eye. Then reattach it to the APD and follow the normal tuning steps with the $1\mu M$ concentration dye sample as usual, keeping in mind you may need to search significantly more than usual to find the correct alignment.

   (e) If there is no signal going through the fiber, check that M2 is flipped down. Then check with a card that signal from L2 is centered and focused onto the fiber entry point denoted by F. Adjust five axis mount on F until a visible signal goes through the fiber. Then proceed as in previous step.

   (f) Ultimate confirmation that this path is well aligned requires that dye calibrations reliably yield reasonable numbers for the focal volume. Check that, then redo alignment as necessary.

   (g) If a lot of alignment was necessary, it is a good idea to check the laser power setting to intensity post-objective calibration as it might have changed. The current one is taped to the side of the box.

3. Camera

   (a) Flip M2 into beam path. Check with a very low laser power setting and short exposure time (if using an acrylic sample) that the signal is on camera.

   (b) If there is no signal, turn up the laser and track the visible signal. M2 should be angled relative to the M1 - L2 optic axis such that the signal is bounced at 90°. This is necessary to prevent CAM

from seeing a skewed or stretched image. Adjust M2 as necessary, then adjust the mounting on CAM to get the signal near the center of the camera.

(c) Focus to a surface on the sample. Adjust the focus up and down relative to this surface and check that the image of the laser spot on camera does not translate or skew.

(d) The camera is now aligned.

3.3 Troubleshooting

The following are the most common issues I have experienced, and for each case a list of the most common causes as a start to the troubleshooting process.

- Calibrate to bad focal width

  1. Is it consistently the same bad value? If so, redo APD alignment.
  2. If it is simply inconsistent, try with fresh sample.
  3. Check what the sample looks like on camera. Focus down to the cover glass. If there is surface binding, make a new sample chamber because it may be a high background problem. Occasionally surface binding manifests as a signal creep over time, for example see Figure 3.4.

- No signal

  1. Check position of M2.
  2. Check on camera with attenuation turned down by one ND. If there is no signal on the camera either then check the sample (how it is mounted, the focusing, and concentration).
  3. If there is signal on camera but it is also unusually low, check alignment.

- Unreasonable size measurements

  1. Sample aggregation. Remake sample chamber.

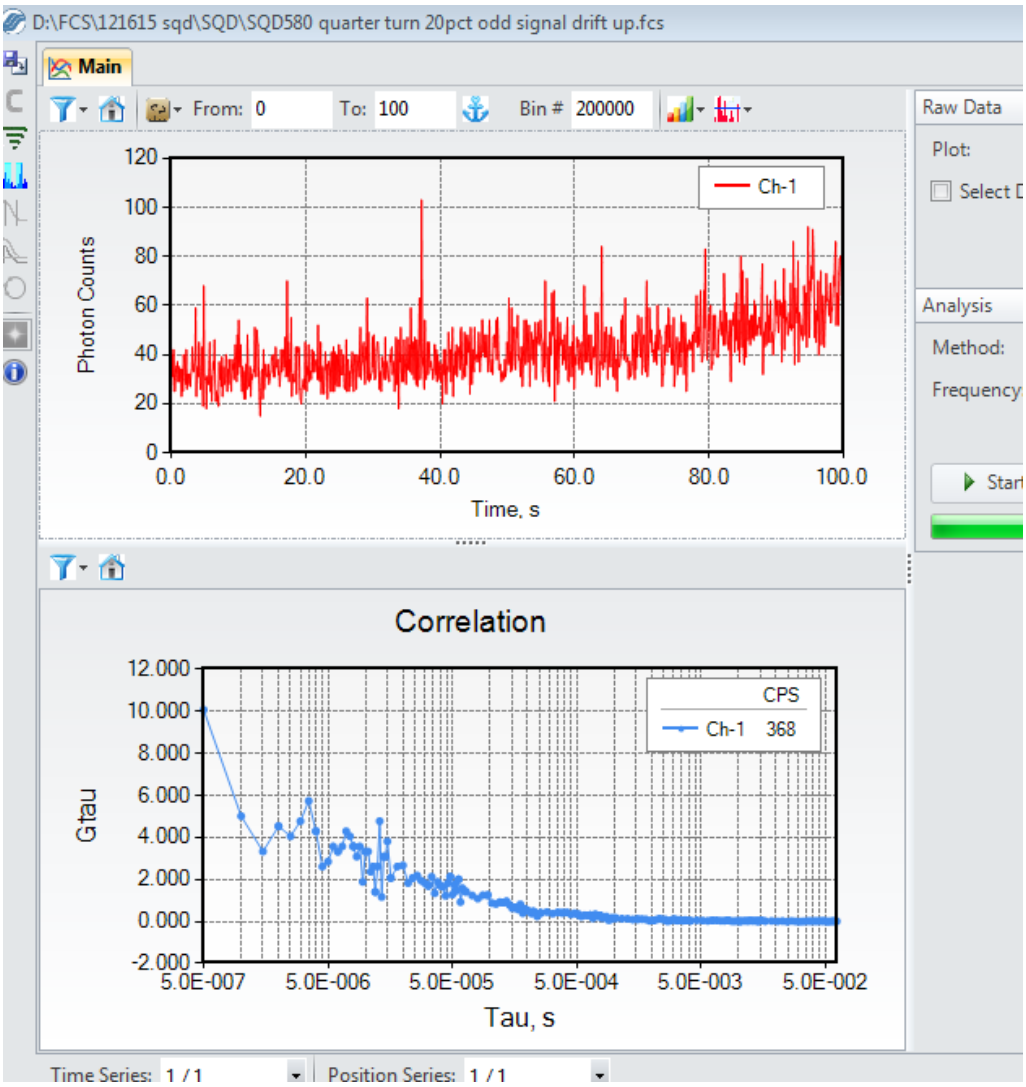

Figure 3.4: An example of the signal level as seen on the APD drifting upwards over time. Top: Raw signal from APD in photons. Bottom: Derived correlation curve from this data.

2. Poor signal to noise. Try again with higher laser power level. The fitting algorithm does not coverage well when noise is high, especially the triplet state fit (Eq. 2.5). When the fitting algorithm fails at least one of the fitted parameters will be suspiciously round values.
3. Quantum dot blinking, to be discussed in Section 5.3. Double check the laser power level is not too high, and use fresher quantum dots if there is still trouble. They tend to get dimmer over time.

CHAPTER 4

MATERIALS AND METHODS

4.1 Quantum Dot Ligand Exchange

To make the small quantum dots in this study, quantum dot core/shells at the desire emission peaks are purchased from vendors in organic solvents typically Toluene. Since they are metallic and lack any coating, they are not soluble in water until coated with an amphiphilic ligand.

The catalog numbers are listed in Table 4.1.

4.2 Buffers

4.2.1 PBS

PBS is short for Phosphate Buffered Saline, a type of minimal buffer. It consists of:

- 10 mM PO_4^{3-}
- 137 mM NaCl
- 2.7 mM KCl
- pH of 7.4

4.2.2 Normal Extracellular Saline

This buffer is isoosmotic with many cell types and therefore is a good approximation to the buffers which the quantum dots will be used in by researchers.

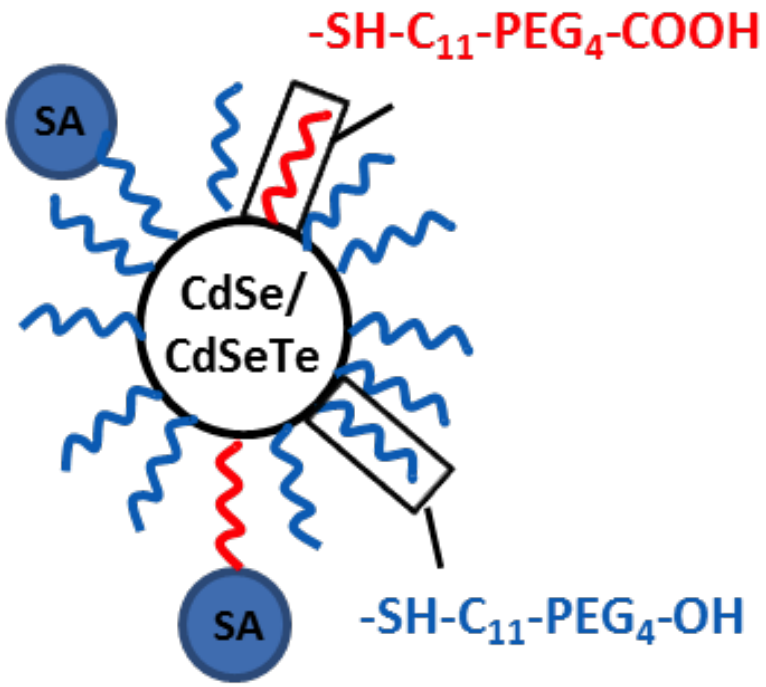

Figure 4.1: The carboxylic and hydroxyllic ligand coating which makes the sQD soluble in water-based buffers. Depending on need, functional groups such as the Streptavidins (SA) shown are attached to the fluorescent probe for specificity in targeting.

Therefore, for most relevance we want to measure hydrodynamic sizes in this buffer.

- 0.87X HBSS
- 10.0 mM HEPES
- 1.0 mM $MgCl_2$
- 1.2 mM $CaCl_2$
- 2.0 mM Glucose
- pH 7.3 - 7.4

where HBSS has composition:

- 0.137 M NaCl
- 5.4 mM KCl
- 0.25 mM Na_2HPO_4
- 0.1g glucose
- 0.44 mM KH_2PO4
- 1.3 mM $CaCl_2$
- 1.0 mM $MgSO_4$
- 4.2 mM $NaHCO_3$

In practice, experimental controls showed that the hydrodynamic sizes measured in this buffer are the same as those measured in PBS or even only 10mM HEPES, the pH-buffering ingredient in Normal Extracellular Saline.

4.3 Dyes and Commercial Quantum Dots

The catalog numbers of quantum dots used in this study are listed in Table 4.1. The quantum dot at emission peak 615 was synthesized by Smith Lab here at University of Illinois.

Table 4.1: Catalog Numbers of Quantum Dots and Dyes Used

Product	**Manufacturer**	**Catalogue No.**
CdSe core emission peak 540	NN-Labs	CZ540-10
CdSe core emission peak 580	NN-Labs	CZ580-10
CdSe core emission peak 600	NN-Labs	CZ600-10
Qdot® 705 ITK™Organic Quantum Dots	Thermofisher Scientific	Q21761MP
Qdot® 545 ITK™Carboxyl Quantum Dots	Thermofisher Scientific	Q21391MP
Qdot® 585 ITK™Carboxyl Quantum Dots	Thermofisher Scientific	Q21311MP
Qdot® 605 ITK™Carboxyl Quantum Dots	Thermofisher Scientific	Q21301MP
Qdot® 705 ITK™Carboxyl Quantum Dots	Thermofisher Scientific	Q21361MP
Qdot® Streptavidin Sampler Kit	Thermofisher Scientific	Q10151MP
Rhodamine 110, Laser Grade, 99%	ACROS Organics™	419075000



Figure 4.2: Example of the basic microfluidic chamber used in this study, comprised of simply a microscope glass slide, a glass coverslip, and two pieces of double-sided tape. Figure adapted from [6].

4.4 Sample Chamber

An FCS instrument illuminates on the order of only one femptoliter of volume, so it actually is common practice to simply drop a single droplet of the sample onto an exposed piece of glass for data collection. For this study to eliminate the effects of sample concentration drift due to buffer evaporation, all experiments were done in microfluidics chambers as shown in Figure 4.2. Here the evaporation can only happen from small openings on the two ends of the channel, and the sample concentration remains stable for even hour long multipart experiments. To prevent surface binding, the cover glass used is chemically treated (PEGylation) prior to assembly, following the protocol in [18]. Furthermore, a $10\frac{mg}{mL}$ dilution of Bovine Serum Albumin is flown into the chamber and incubated for further coating just prior to flowing in the real sample.

Control experiments show that our sample chamber yields the same results as a drop of sample on exposed glass, but that our samples last long past the drop begins to evaporate, in about ten minutes.

4.5 Troubleshooting

The following are a few common issues pertaining to the sample, and possible causes.

- Visible directional flow on camera: this is more likely than not an indication that the sample chamber is leaking. Either the sample is too old and evaporation has happened from the ends of the chamber

to reach your field of view, or the chamber was made poorly to begin with.

- Higher than nominal background counts:

    1. The concentration may be too high. Switch to camera and check that you see a haze (for dyes) or about one particle per second drifting into view (for quantum dots).
    2. Focus down to coverslip surface and check for bound particles.
    3. Check for light leaks.

CHAPTER 5

RESULTS AND DISCUSSION

5.1 DLS Tests

All measurements were performed on a Zetasizer Nano (Malvern).

We chose three samples to measure by DLS; two different fluorescent beads at nominal sizes 24nm and 43nm with emission peaks far enough from that of the instrument's light source, 633nm, that fluorescence and absorption effects should be minimal, and also a commercial quantum dot with emission at 605nm, where we expect fluorescence and absorption to be non-negligible. All samples were sonicated for five minutes to break up any present aggregates after dilution. In two out of three cases the number- and volume-distributions yielded mean sizes which differed by a factor of two (Table 5.1).

In general the lack of agreement between the different means suggest some amount of aggregation, and the number distribution which gives least weight to oversized aggregates best reflect the size of single particles. However the measured size by this distribution of the quantum dot of 12.2nm is significantly lower than manufacturer's specifications of 16.5nm, consistent with the wavelength-dependent effects leading to an underestimation of size. This

Table 5.1: Dynamic light scattering measurements, shown as mean of five measurements ± standard deviation.

	Hydrodynamic Size (nm)		
	Intensity Mean	**Number Mean**	**Volume Mean**
Fluosphere yellow-green	$294.2 \pm 22.2nm$	$15.0 \pm 1.7nm$	$33.1 \pm 3.7nm$
Fluosphere orange	$66.4 \pm 1.2nm$	$38.5 \pm 0.8nm$	$48.7 \pm 0.6nm$
bQD 605nm	$266.4 \pm 58.1nm$	$12.2 \pm 0.5nm$	$36.4 \pm 11.2nm$

effect is well-documented by the manufacturer [25] and is consistent with published data of other groups, for example that of Choi et. al. [19], in which DLS measurements are presented alongside GFC measurements for multiple colors of quantum dots.

5.2 FCS Controls

5.2.1 Consistency of Focal Volume Width Calibration Using Different Dyes

Referring back to Equation 2.3, the FCS focal volume width r_0 can be calibrated with any dye or fluorescent particle for which a trusted independent measurement of the diffusion coefficient D exists in literature. Up to date values of D is such a common need within the FCS community that lists of them exist, for example as found in [36]. The calibrated r_0 should be independent of the dye used if the calibration is robust. The following is a comparison of calibrations done with four different fluorescent dyes, Rhodamine 110, Rhodamine 6G, Cyanine 5, and Fluorescein.

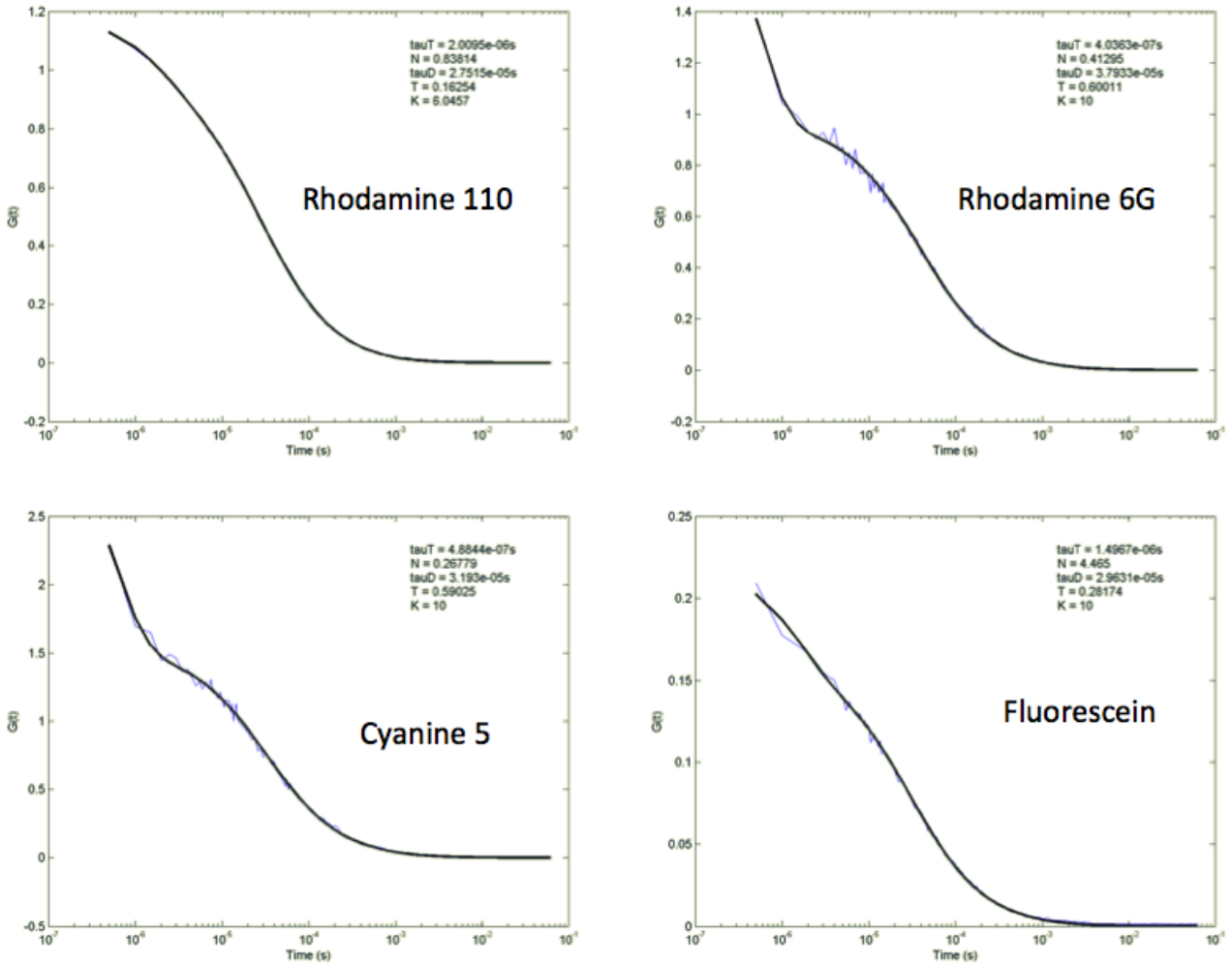

Figure 5.1: Calibration with four different dyes, Rhodamine 110, Rhodamine 6G, Cyanine 5, and Fluorescein.

With the fitted τ_D values in Figure 5.1 and D values from [36], plug into a slightly rearranged Equation 2.3

$$r_0 = \sqrt{4\tau_D D} \tag{5.1}$$

. . . to get the following calibrations for r_0 :

$$\begin{aligned} r_{r6G} &= 255.3nm \\ r_{rh110} &= 227.3nm \\ r_{Cy5} &= 214.3nm \\ r_{Fluorescein} &= 224.3nm \end{aligned}$$

These values are extremely consistent with the exception of rhodamine 6G, which may simply be less uniform in size than the others. These results justify confidence in the calibrations, and are a large reason why rhodamine 110 was ultimately chosen as the calibration dye. To calibrate with four dyes daily would be too much, so only one is typically used.

5.2.2 Optical Saturation Threshold of Rhodamine 110

One implicit assumption in the analysis of FCS data is that a three-dimensional Gaussian excitation volume implies the emission intensity is also a three-dimensional Gaussian. This is only true if the particle does not undergo optical saturation, where above a certain excitation power threshold the emission response no longer is linear to further excitation. It is easy to empirically determine this threshold, by stepping up the excitation power while monitoring the emission signal. The results of this is shown in Figure 5.2. Informed by this, calibrations for all further presented data where conducted at laser power setting 50% at neutral density setting 3.

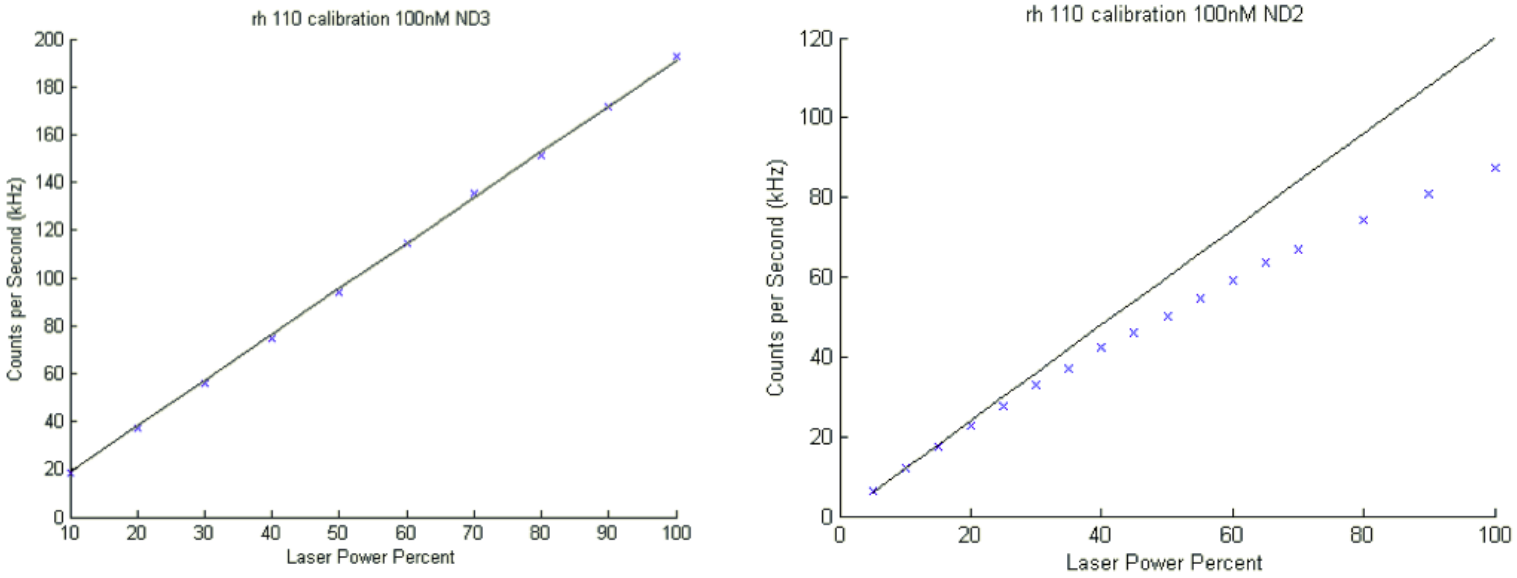

Figure 5.2: Emission response of a rhodamine 110 dye sample in the FCS, with the laser attenuated by neutral density of 3 on left and 2 on right. This data shows the dye response is linear up to laser power 15% at neutral density, roughly equivalent to 150% at neutral density 3.

Optical saturation also occurs in quantum dots, but it is convolved with another excitation power dependent effect: blinking. This will be explored in the next section.

5.3 Laser Power Dependence vs. Core Composition

Prior studies of quantum dot size using FCS reported size dependence on blinking characteristics [37, 38] and saturation [39]. To quantify these effects on our particular samples we measured size as a function of laser power post-objective for two CdSe/ZnS core/shell quantum dots, the primary core type used in this study, one CdSeTe/ZnS core/shell quantum dot, and one CdTe/ZnS core/shell quantum dot not used in our synthesis but included for direct comparison against the results reported in De Thomaz et. al, where this type of quantum dot was used exclusively [37]. The resulting data is presented in Figure 5.3.

It was found that the differing photophysics of the three core/shell types led to different laser power dependence in the size measurements. The CdSe core quantum dots suffered the least effects and across the two samples measured was consistent in measured size over two orders of magnitude of laser power (1μW to 100μW). In stark contrast, we observed a dramatic decrease in measured size with laser power for the CdTe core, reproducing the results of De Thomaz et. al, and a dramatic increase in measured size with laser power for the CdSeTe core [37]. Informed by these findings, we limit our laser power to 1μW post objective for CdSe core quantum dots and to 0.3μW post objective for CdSeTe core quantum dots for all reported measurements to follow. These maximum laser powers are indicated in the inset to Figure 5.3 as dotted vertical lines, with CdSeTe in red and CdSe in black. Our data suggest that limiting laser power to 0.3μW for our CdSeTe core quantum dots limits the associated size error to 5%. Due to a lack of signal we were unable to acquire reliable data at lower laser powers.

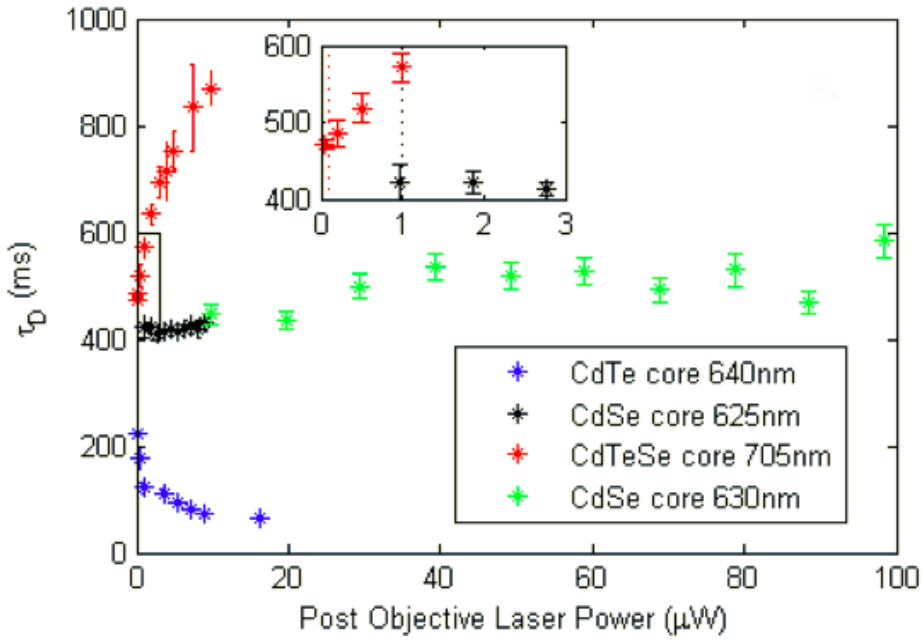

Figure 5.3: Plot of measured diffusion constant τ_D as a function of excitation laser power post objective. (Inset) Vertical dotted lines indicate maximum laser power used in this study for CdSe core quantum dots (black, 1μW) and CdSeTe core quantum dots (red, 0.1μW).

5.4 Effect of Modified Coating on Particle Size

We synthesized quantum dot probes at four different emission peaks (545nm, 585nm, 605nm, 705nm) using our encapsulation scheme as shown in Figure 4.1, with carboxyl surface and also functionalized each with streptavidin. For each case we compared the size of the resulting quantum dot against that of the closest match in emission spectrum that is commercially available from Thermofisher Scientific (formerly Invitrogen).

Test sampled exhibited varying diameter variation within the population, and to determine the hydrodynamic diameter to the desired accuracy at least N = 20 FCS measurements were taken for each sample. Whenever possible all data points in each set were taken of particles from a single synthesis procedure, to eliminate unnecessary variables. Each FCS measurement of τ_D results from a time correlation trace over 100s, analyzed as 10 separate 10s traces to check for variation on the timescale of seconds which would indicate the presence of micro-aggregates manifesting as rare high intensity outliers. For each of the emission peak in this study, four different samples

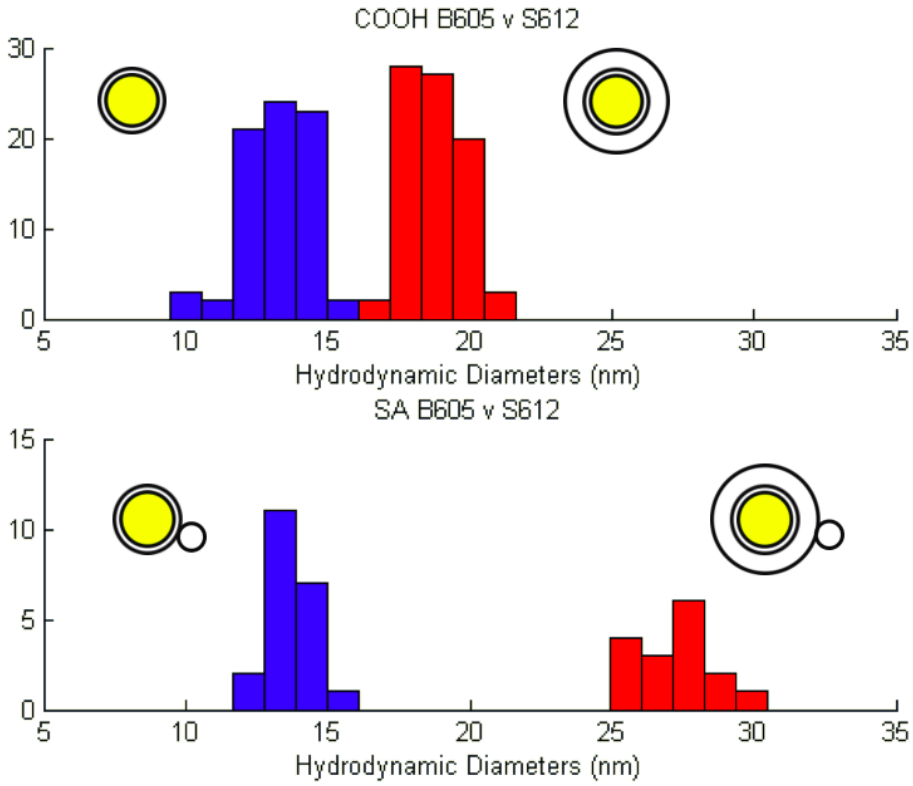

Figure 5.4: Measured hydrodynamic diameters of quantum dot probes of emission peak 612nm (lab-made sQD) and 605nm (commercial). **Top**. Without SA, sQD in blue and commercial bQD in red. The distributions are distinct with no overlap, with the lab-made version . **Bottom**. With SA.

were measured: lab-made (carboxyl) with and without conjugation to Streptavidin, commercial with and without conjugation to Streptavidin. Each set of measurements yields a single-mode distribution from which a peak and the corresponding standard deviation can be determined. As an example, the histograms corresponding to probes of emission peak 605/612nm is shown in Figure 5.4.

In order to compare the diameters of the different probes against each other, the mean and standard deviation for each population are plotted as a bar in groups by emission peak, this is shown in Figure 5.5.

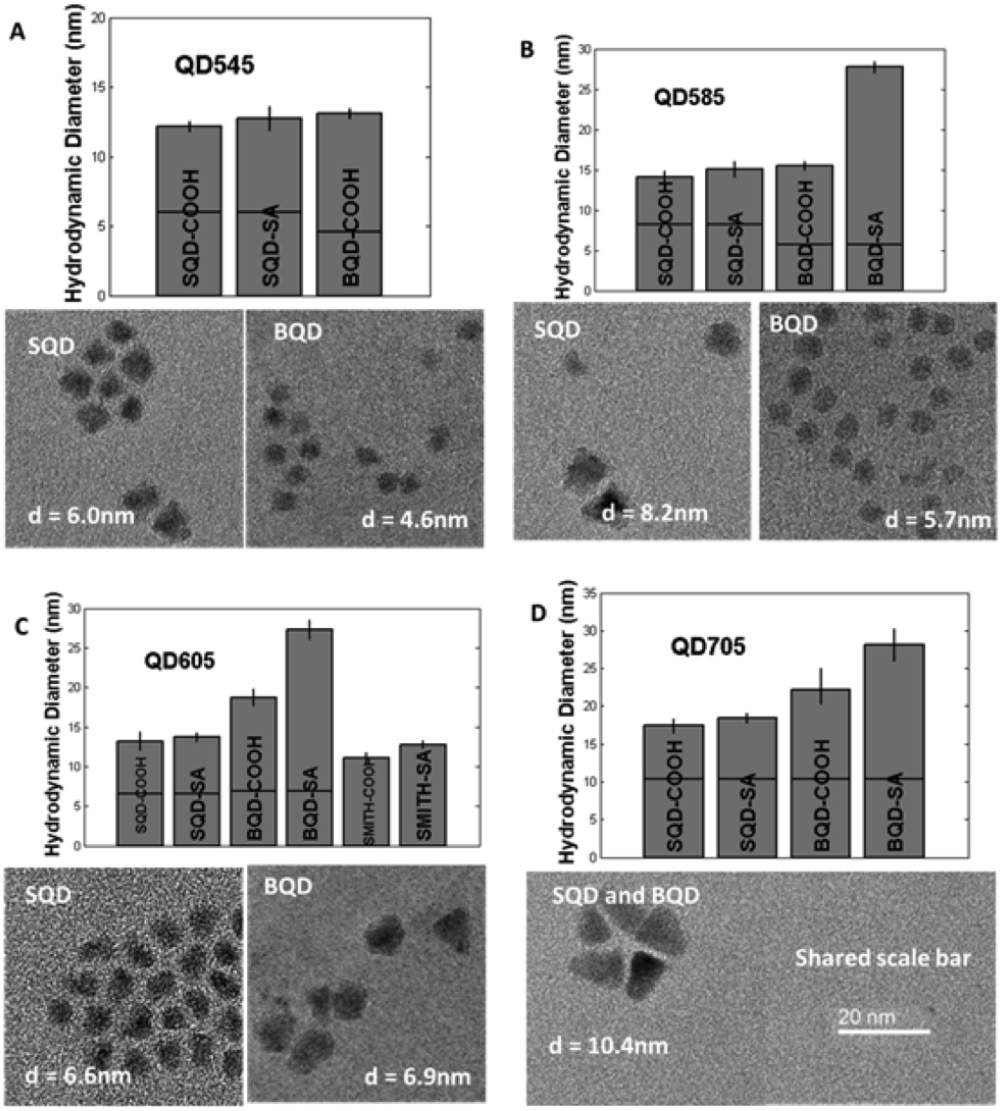

Figure 5.5: Hydrodynamic diameters of quantum dot probes arranged by emission peak, with transmission electron micrographs from which we determined the contribution to final size by the core/shell. Core/shell diameter are indicated on the bars as horizontal line where available. **A**. 540-545 nm peak emission. **B**. 580-585nm peak emission. **C**. 605-615nm peak emission. Fifth and sixth bars denote additional core/shell synthesized in Smith Lab. **D**. Emission peak 705nm. In this case all four quantum dots were synthesized from same core/shell.

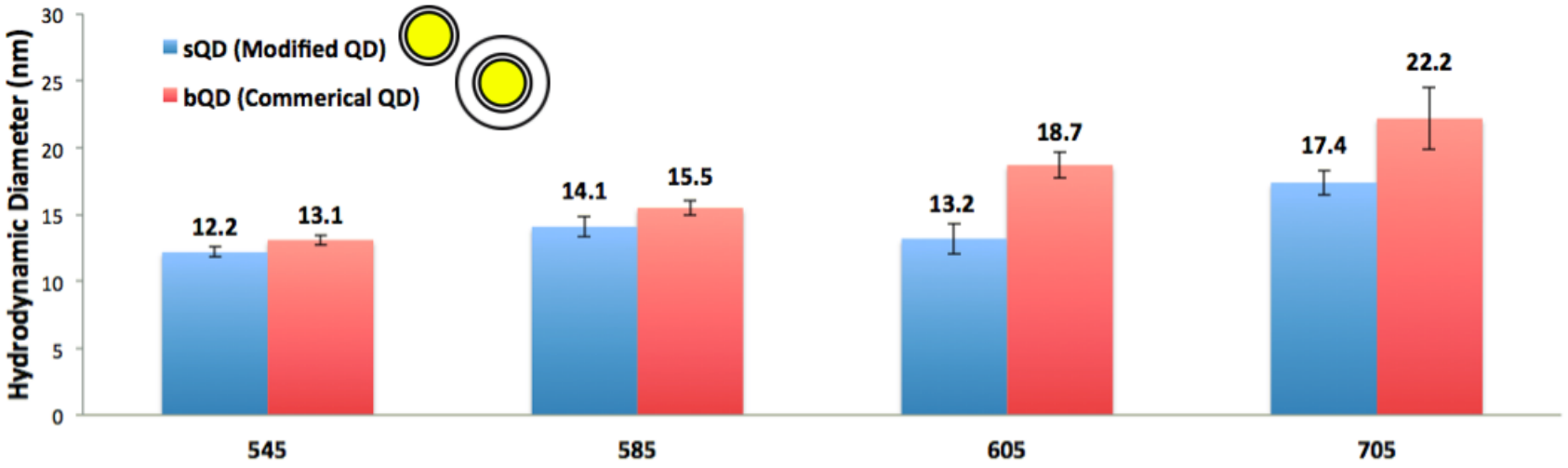

Figure 5.6: FCS-measured hydrodynamic diameters for the carboxyl coating only samples, which have not undergone conjugation with Streptavidin. Lab-made, modified quantum dots shown in blue, the equivalent commercially purchased variant in red. Vertical bars indicate ± one standard deviation computed from the number of data points N.

For the samples without the additional step of conjugation to Streptavidin, where our modified coating should be the sole contribution to any differences in hydrodynamic diameter, a variable decrease in size is observed from 0.9nm (545nm emission peak) to 5.5nm (605nm emission peak). Our measurement of 605nm emission peak commercial quantum dot is consistent with previous publications [40]. To facilitate these comparisons, the measured diameters are replotted in with-SA and without-SA pairs in Figure 5.6.

At first glance at least the two results, at emission peaks 545nm and 585nm, where the diameter decreased only by 0.9nm and 1.4nm, respectively, are far too small to be consistent with the expected diameter decrease due to the decreased length of the ligand compared to the polymer shell of the commercial variant. While the exact chemistry of the commercial variant is proprietary and therefore not known, we expected a diameter decrease of 3-5nm. Furthermore, the difference in hydrodynamic diameter should not depend on the emission spectrum of the quantum dot, as the current data suggests. Transmission Electron Micrographs of all the samples, representative subsets of each shown in Figure 5.5, show clearly an unaccounted for variable – a non-negligible difference in size between core/shells from NN-Labs, used for the lab-made variant, and Thermofisher Scientific, in the commercial variant, despite the near-identical spectra. In consequence, the quantum dot cores used for the lab-made variant are two cases larger than the corresponding core of the commercial variant by more than a nanometer. To isolate the hydrodynamic size from the encapsulation layer this differing core/shell size must be taken into account when drawing conclusions from the measured sizes of the entire probe. The core/shell contribution to size are indicated as the bottom portion of each bar graph. It is then clear that the altered encapsulation corresponds to a diameter decrease of 2.3nm (545nm emission), 3.9nm (585nm emission), 5.2nm (605nm emission), 4.8nm (705nm emission). The core-subtracted diameters are replotted in Figure 5.7 for clarity.

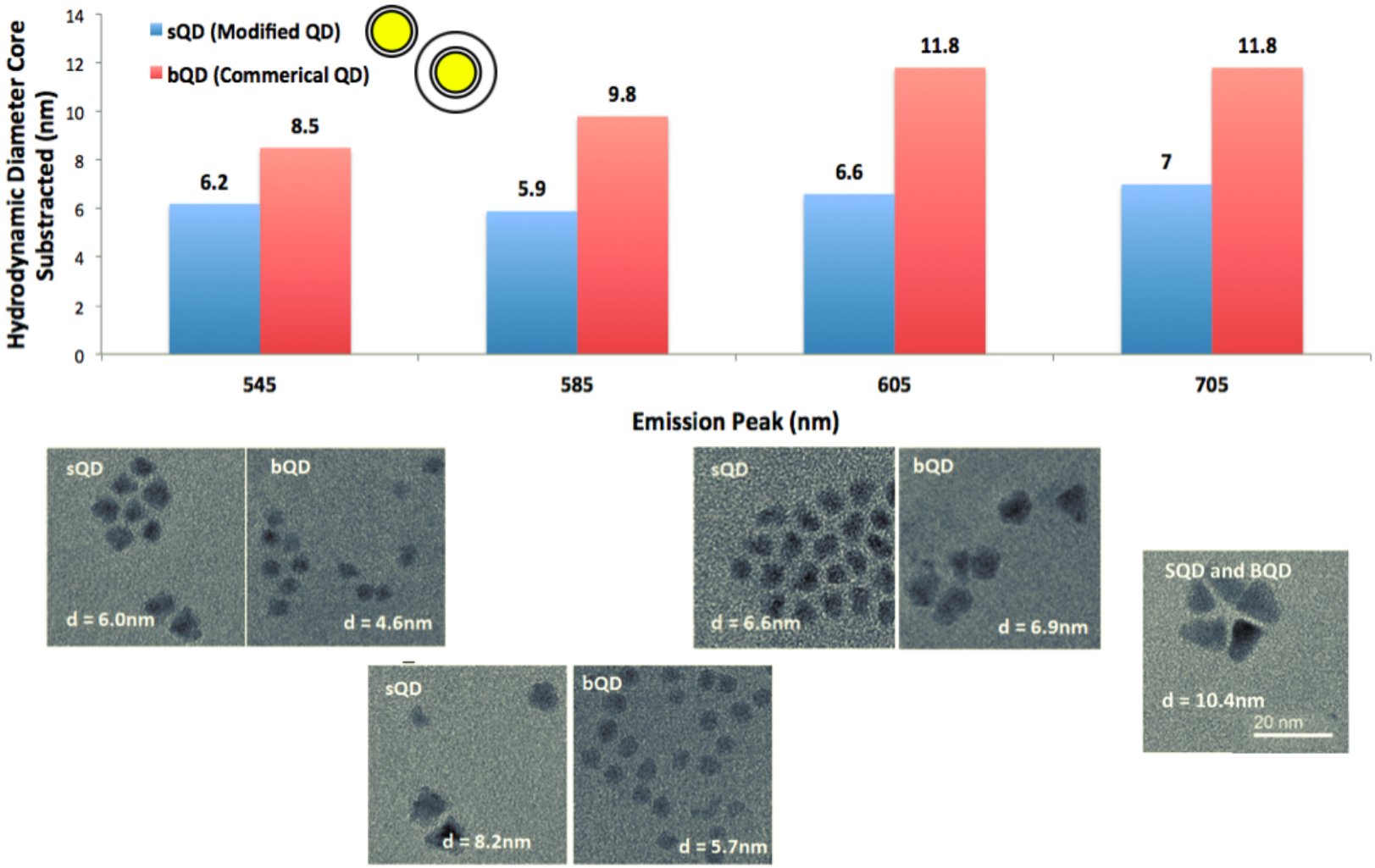

Figure 5.7: **Top**. FCS-measured hydrodynamic diameter with TEM-measured core diameters subtracted, to isolate the effect of the modified coating. **Bottom**. TEM data as previously shown in Figure 5.5 included here for ease of reference.

Though this assures use that the chemistry relating to the modified coating worked as anticipated, it still remains to be explained how the small hydrodynamic size difference on the full encapsulated quantum dot could yield the qualitatively and quantitatively distinct behavior observed when these probes were used as labels in a cellular setting. However, keeping in mind that any probes used as cellular labels would have been conjugated for labeling specificity, and therefore much more closely approximated by the Streptavidin-conjugated test samples, the measurements for those samples are presented in an analogous manner in Figure 5.8.

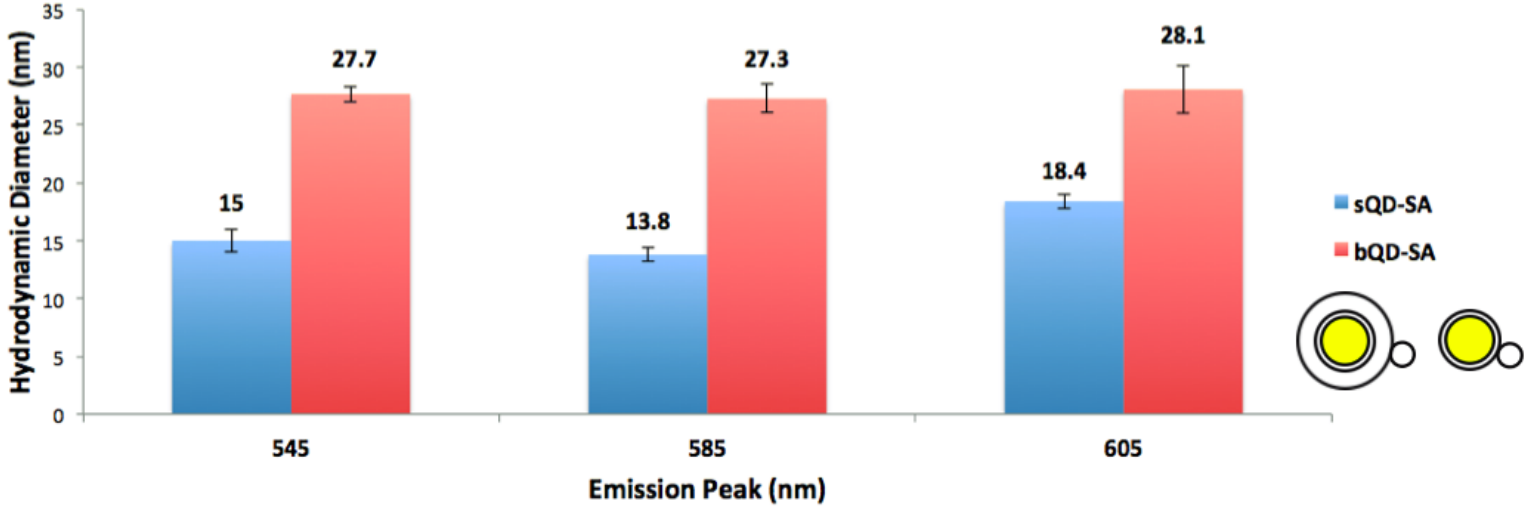

Figure 5.8: FCS-measured hydrodynamic diameters for the Streptavidin-conjugated samples. Lab-made, modified quantum dots shown in blue, the equivalent commercially purchased variant in red. Vertical bars indicate ± one standard deviation computed from the number of data points N.

In all cases the streptavidin-functionalized quantum dot probe is larger than its non-functionalized, carboxyl surface counterpart. For the quantum dots we synthesized, this size difference is consistently between 0.5nm and 1.0nm. For the quantum dot core/shell synthesized in Smith Lab, this difference was 1.7nm (this data was shown in Figure 5.5 but omitted in subsequent figures.) In comparison, for the commercially purchased quantum dot probes the Streptavidin functionalization correlated with a multi-nanometer increase in size in all three cases where the comparison was made.

We attribute this largely to two factors: an increased tendency for the commercial probes to form micro-aggregates, and the commercial probes being functionalized with a greater number of Streptavidins on average. Regarding the first, unlike aggregates of the order of ten or more number of particles clustered together which appear in the raw intensity trace as easy to filter peak which are clear outliers, micro-aggregates consisting of clusters of two to five particles could pass through a filter by intensity threshold. Upon computation of the time correlation, the fluorescence signal from these large, and therefore slowly diffusing, micro-aggregates will fall on the high-τ end of the curve, distorting the distribution from that as predicted by Equation 2.2, which assumes a test sample consisting of a single size population. Large intensity spikes and relatively poor fit to Equation 2.2 was indeed observed in the raw intensity datasets for the commercial Streptavidin-conjugated probes with much higher frequency than the unconjugated quantum dots, both indicators of a polydisperse sample. As for the second, the optimal number of Streptavidin, or in general the optimal number of any applicable functionalization group, depends on the intended use. This average value affects the Poisson statistics when these probes are allowed to bind with their labeling targets by setting the number of available binding sites. In situations where unbound probes either could not be removed from the experimental system or could only be removed with great difficulty, a greater average number of functional groups is used to be certain a negligible number of probes were conjugated to zero functional groups and therefore will end up unbound. Since the functionalization reaction involves incubation of the unlabeled probe with the functional groups, the number of functional groups per completed probe also follow the Poisson Distribution, and a higher than otherwise desired mean value must be targeted in order to suppress the probability of the tail end corresponding to zero functional groups. In the next

Section the estimation of these average numbers of Streptavidins using the diameter measurements is presented and discussed.

5.5 Calculation of Number of Streptavidin per QD

Comparing the measured hydrodynamic size of non-functionalized versus Streptavidin-functionalized sQD, one can compute the change in volume. Then assuming this entire change in volume is due to the Streptavidins (SA) bound, and using the accepted value of hydrodynamic diameter 4nm per unit of SA, it is possible to estimate the average number of SA per sQD. The following is one such calculation using FCS measurements of sQD620.

$$
\begin{aligned}
d_{sQD620} &= 13.2 \pm 0.12nm \\
d_{sQD620-SA} &= 13.8 \pm 0.12nm \\
\Delta V_{Hydrodynamic} &= \frac{4}{3}\pi \times \left(\left(\frac{d_{sQD620-SA}}{2} \right)^3 - \left(\frac{d_{sQD620}}{2} \right)^3 \right) \\
&= \frac{4}{3}\pi \times 41.01 \\
\Delta V_{perSA} &= \frac{4}{3}\pi \times \left(\frac{4}{2} \right)^3 \\
&= \frac{4}{3}\pi \times 8 \\
&\Rightarrow \approx 5\text{SA per sQD620 on average}
\end{aligned}
$$

We note that though the exact synthesis procedure for the Thermofisher Scientific quantum dots are proprietary and therefore unknown, they provide an estimate of 5-10 streptavidins per quantum dot for their conjugates. This is consistent with the value computed above. However carrying out this same calculation for the other FCS data presented before typically yield a number of SA per sQD in the 1-3 range.

5.6 Summary

In this study we have shown that quantum dot core/shells encapsulated with the amphiphilic ligand C11-(PEG)4- show a decreased hydrodynamic size,

a property which is increasingly important for their use in cellular studies. Due to the cost of decreased robustness associated with minimizing hydrodynamic size, we compared measurements by fluctuation-based techniques fluorescence correlation spectroscopy and dynamic light scattering. Dynamic light scattering is convenient and for many samples provide a size measurement within a few nanometers of those from well-established chromatography techniques. However the measurement error is difficult to calibrate. For applications where more accuracy is necessary, we recommend fluorescence correlation spectroscopy as an alternative.

Part II

CHARACTERIZATION OF DIFFRACTION GRATINGS WITH THE LONG TRACE PROFILER

CHAPTER 6

INTRODUCTION

6.1 Synchrotron Optics, Specifically Diffraction Gratings

Synchrotrons are a far departure from the microscopes discussed in the previous part of this thesis. However for biophysicists, specifically x-ray crystallographers, they are relied on to serve a similar role in the researcher's arsenal – to measure tiny distances with light. While fluorescence microscopes are bench top instruments, synchrotrons are immense, billion-dollar structures the size of a football field, maintained and operated by dedicated teams of scientific staff and funded at the national level. Within their storage rings an electron beam traveling at near the speed of light radiate as it navigates through the turns. This emission, termed synchrotron radiation, is as powerful as could be found in a laboratory setting, with wavelengths from 100nm to as low as $1\mathring{A}$.

These light pulses, in the x-ray range of the spectrum, are shaped and directed by various specialized optics from their source to the user end station where researchers conduct their experiments. One type of optic, the diffraction grating, spreads out the frequency bandwidth components of the beam in space, thus allowing a narrow bandwidth to be selected for experiments by the insertion of a simple slit. In general, the higher quality diffraction grating, the wider it can split the source light so the bandwidth could be filtered to higher precision. And since virtually all measurements made with light is a function of wavelength, the quality of this optic has real consequences for instrument performance.

It is the characterization of these optics which is the focus of Part II of this thesis. In particular, the United States Department of Energy synchrotron radiation facilities, consisting of Argonne National Laboratory (Advanced

Photon Source), Lawrence Berkeley National Laboratory (Advanced Light Source), and Brookhaven National Laboratory (National Synchrotron Light Source-II), lacked the ability to perform critical metrology on a specific type of diffraction grating, the varied-line spacing (VLS) grating. The goal of the project presented here is to develop this capacity by expanding an existing ultra-precision instrument, the Long Trace Profiler (LTP), and to service the community by performing metrology on diffraction gratings to be installed in Brookhaven National Laboratory's planned Soft Inelastic X-ray Scattering (SIX) Beamline due to be completed in 2017.

This chapter will lay out the necessary background information. VLS diffraction gratings will be discussed in Section 6.3), and the LTP in Section 6.3).

6.2 The Textbook Diffraction Grating

A diffraction grating redirects a beam of light through an interference effect, as opposed to reflection for mirrors and refraction for lenses. Parallel lines or grooves across the surface of a diffraction grating act as secondary sources of light when illuminated by an incident beam, and the resulting summation for intensity is constructive versus destructive as a strong function of angle.

Traditionally the distance between adjacent grooves in a diffraction grating is denoted by d, and for the basic diffraction grating d is constant across the full optic. This spacing d, along with λ the wavelength of the incident light, are sufficient to determine the angles θ at which the optical path length difference between light emerging from adjacent lines will constructively interfere [3, 41].

As depicted in Figure 6.1, consists of two contributions, each from a right triangle with hypotenuse of length d, and opposite angles equal to θ_i and θ_d respectively. Thus the condition for diffraction angles θ_{dm} at which constructive interference occurs given incidence angle θ_i is summed up in Equation 6.1:

$$d(sin(\theta_i) + sin(\theta_d)) = m\lambda \tag{6.1}$$

It is immediately apparent from the above equation that for a given θ_i,

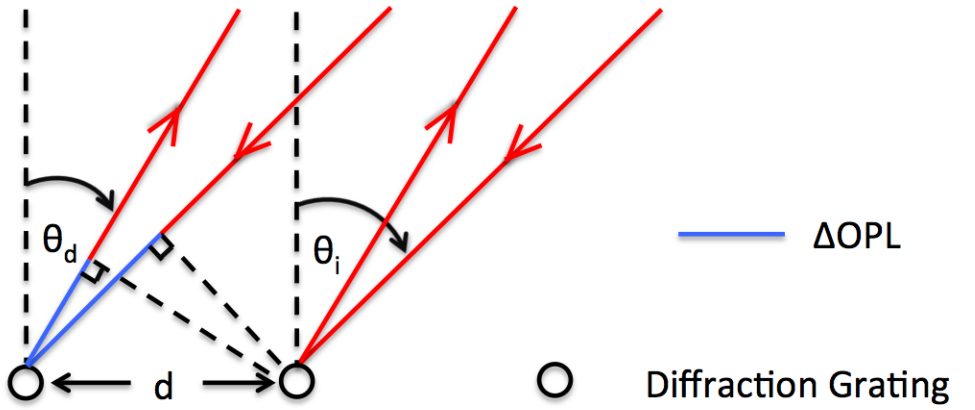

Figure 6.1: In the simplest case where $\theta_i = 0$ for normal incidence, the first diffracted order $m = 1$ emerges at the angle θ_d where between adjacent lines is exactly one wavelength.

there can exist one value of θ_d for more than one integer value of m, and that m could take on negative values with the corresponding angles falling on the other side of the surface normal. The integer m is referred to as the order. In the special case m = 0 Equation 6.1 reduces to the well known law of reflection, $\theta_i = \theta_d$ (in this case more appropriately labeled θ_r).

For full generality it must be mentioned that transmission diffraction gratings , where the diffracted beam emerges on the other side of the diffraction grating from the incident beam, also exist. Here we restrict discussion to reflection gratings as they are the only type found in synchrotron settings due to their significantly higher possible efficiencies and lower distortion. Outside of synchrotron beam lines, reflective diffraction gratings can be readily found in any monochrometer where they serve to decrease bandwidth, in spectrometers where they allow scans across wavelength, and many laser cavities where they aid in frequency tuning.

One implication of Equation 6.1 is that the incident light intensity is divided among multiple outgoing beams, as in any relevant situation there will be at least a zeroth order (reflected beam) and plus and minus first orders out of the diffraction grating. (It is certainly possible to look at a reflection type diffraction grating at normal incidence and see only the zeroth order reflection, but then you would be much better off with a plain mirror.) When there are no restrictions on the light source providing the incident intensity,

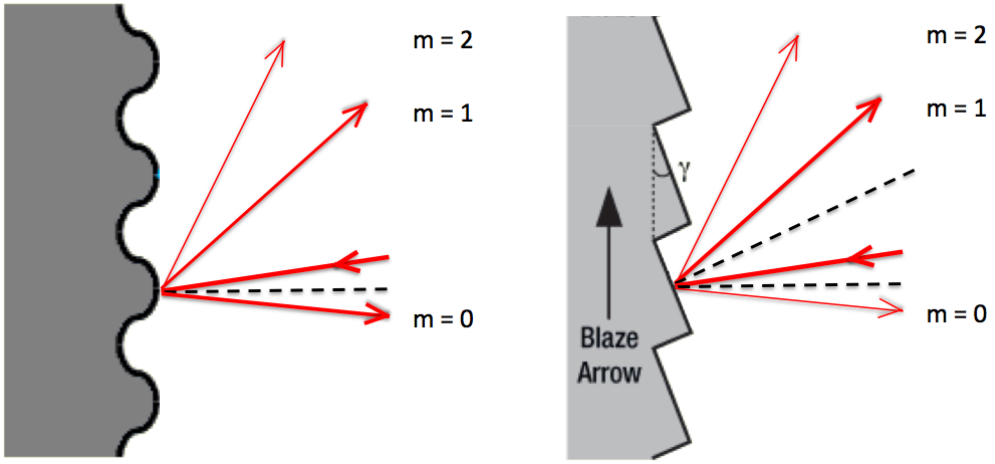

Figure 6.2: Left: Diffraction grating with sinusoidal profile, intensity decreases with diffraction order. Right: A blaze grating optimized for efficiency in the first order. Figure modified from Thorlabs.

for example in basic monochromators where the light comes from a bright lamp, the main concern is to block off the unwanted orders. However in applications which place a stringent requirement on efficiency, as is the case in synchrotron use, the outgoing intensity distribution is optimized for a specific order by a modification to the height profile of the grooves in the diffraction grating. The strategy is quite simple – once θ_i and θ_d are known, one can then make the grooves into a sawtooth profile which maximizes the surface area at the correct tilt such that the reflected beam also leaves at $\theta_r = \theta_d$. The difference between the groove shapes is illustrated in Figure 6.2. Such diffraction gratings are referred to as blazed gratings.

6.3 The VLS Diffraction Grating

A perfect blazed grating is as efficient as the diffraction grating itself can be. But in situations where extraordinary efforts are made to maximize efficiency, diffraction gratings are further engineered to also perform the function of a lens or curved mirror – to change the collimation of the beam. No optical element is one hundred percent efficient, even a custom optic which took a year to produce, so to eliminate the need for another optic to be inserted into the path is equivalent to a small efficiency gain. The way this is done

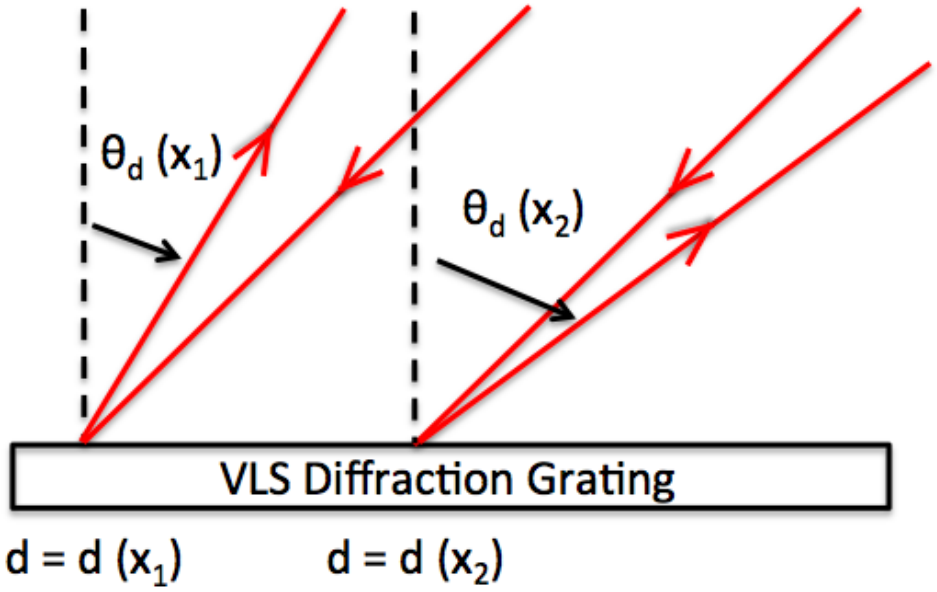

Figure 6.3: When illuminated by light at a constant angle of incidence, a VLS grating will send out diffracted rays at different angles θ_d, determined by the local line density $d(x)$ at the location where the diffraction event occurs.

is to vary the groove spacing d across the pattern of the diffraction grating. This would make θ_d a function of distance x along the pattern.

As illustrated in Figure 6.3, when illuminated at a constant θ_i across its entire pattern, a VLS grating diffracts the light at slightly different angles depending on where on the pattern a specific ray of light hit. Therefore instead of each diffracted order being a plane wave as in the constant line spacing case, for a VLS grating the wavefront of the diffracted order can be made to come to a focus or to diverge from a focus. It is customary for the line density N of a VLS grating to be specified as a third order polynomial function in x, the distance going across the pattern.

6.4 The Imperfections Textbooks Do Not Describe

This is a metrology project, and so it is actually more important to discuss the ways in which a real world diffraction grating can be imperfect than how the textbook version works. For this, it is informative to look into the manufacturing process of diffraction gratings.

The basic, non-blazed diffraction grating is typically made holographically. A periodic interference pattern can be formed by intersecting two laser beams, where the wave nature of light itself can be relied on to set the distances with extreme accuracy. It is then recorded onto a photosensitive material, and the end product is a diffraction grating which is nearly error-free. Since ultimately in this case any error can be traced back to quality of the laser beams themselves, they are often of magnitudes difficult for any light-based instrument to see. This method is also very high-throughput – many diffraction gratings could be manufactured with just a single interference pattern. The low error and low cost makes holographic diffraction gratings extremely popular.

There is, however, one big limitation. Light waves are sinusoidal and so are the interference patterns, leading to sinusoidal groove profiles. It is possible to generate other groove profiles by summing multiple sinusoidal patterns, but to make a good blaze by this method is virtually impossible. For this reason all synchrotron diffraction gratings are either mechanically ruled, or replicated from a mechanically ruled master.

The mechanical ruling process involves a tool being physically dragged across the metallic surface deposited onto a flat substrate to form each individual groove. Considering that a synchrotron diffraction grating has on the order of one hundred thousand grooves, the process takes weeks, sometimes even months. All sorts of mechanical errors can and do occur, for example temperature-induced drifts, contamination, translation stage not traveling true to desired axis, just to name a few. These errors in turn cause quantifiable errors in the diffraction grating which decrease performance, of which the following two are most relevant.

6.4.1 Blaze Angle Errors

Whenever the tool wobbles, the blaze angle will fluctuate. In bad cases the groove profile may no longer resemble that of the ideal sawtooth. Due to the spatial scales involved – tens of nanometers to one micron – the Atomic Force Microscope (AFM) can spot check areas a few micron squared at a time. From such a scan the actual height profile of the diffraction grating surface could be visualized, with an example shown in Figure 6.4.

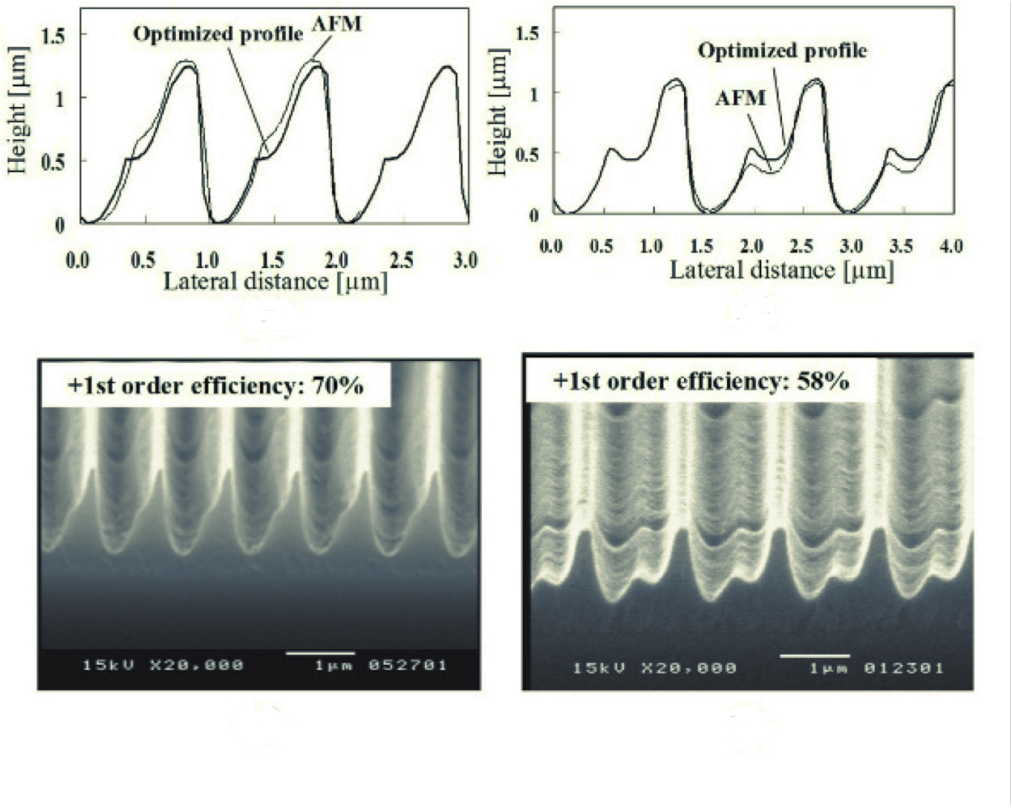

Figure 6.4: Atomic Force Micrographs of two different diffraction gratings, showing the complex height profiles which could be possible. Figure slightly modified from [42].



Figure 6.5: First diffracted order of a diffraction grating when illuminated by the expanded HeNe laser at $\lambda = 532$nm of the Diffractometer, showing obvious variation in efficiency. Visible streaks are common in mechanically ruled gratings.

To scan the entire pattern area would require on the order of ten million AFM fields of view (10mm by 100mm pattern area, 10 by 10 scan area), which is clearly impractical. The standard procedure is to estimate the amount of variability from the spot checks. In terms of quantifiable performance loss in the diffraction grating, deviation of the blaze angle away from the optimized value means decreased local scatter efficiency at the relevant angles. As discussed in Section 6.2 all the scattered light undergo interference, and so it is an intractably difficult problem to compute the exact effect of small variances of the blaze angle.

In extreme cases, for example when dust or debris change the blaze angle abruptly, the resulting efficiency drop is so large it causes a clear intensity drop in the diffracted order. Figure 6.5, taken on the Diffractometer to be discussed in Section 7.1, is an example of a bad but not unusual such case. However, as the illumination wavelength is much different from the X-ray wavelengths the optic is to be used at, the efficiency profiles will in general be different.

6.4.2 Line-Spacing Errors

The second class of errors are errors in the line position, d. This error can be absolute, as in how far the position of the Nth groove of a diffraction grating

of constant line spacing d is from its ideal location (N-1)×d, or relative, as in how far the groove is from its two nearest neighbors. The nature of diffraction means the relative position is the important one.

Acknowledging that d is a function of x means that in Equation 6.1 the variable θ_d will also be a function of x. Therefore line position errors introduce angular divergence into the diffracted orders. There are direct analogs for VLS gratings, with the slight complication that errors in d are deviations from a polynomial function of x with specified coefficients.

In a laboratory setting it is possible to set θ_i and to measure θ_d carefully. From these measurements d could be mapped across the diffraction grating pattern by way of Equation 6.1, which implicitly assumes that all of the grooves are identical. Thus, in practice, errors in blaze angle and in line position are convolved into errors of θ_d, and derived line spacing errors will contain contributions from blaze angle errors.

CHAPTER 7

EXISTING METROLOGY INSTRUMENTS

As new generation synchrotron – better in part due to improvements in optics – so does the metrology capability need to be improved to resolve the increasingly small deviations from ideal specifications and performance [43, 44]. For years VLS diffraction gratings were installed into a beamlines without independent confirmation (by the US National Laboratory synchrotron facility) that the manufacturer did indeed deliver on the specifications. The alternative was to rely on the only facility in the world which could perform this metrology, SOLEIL synchrotron near Paris, often with waiting times of months. Given the complexity of a synchrotron beamline, it is unrealistic to add in such a long lead time for just one component.

More often than not, the expensive diffraction grating, typically one hundred thousand dollars, is indeed to specifications and the commissioned beamline functions as expected. When debugging is required, however, as was the case recently at the IEX beamline at Argonne's Advance Photon Source, the entire beamline had to be taken offline for the diffraction grating to be uninstalled out of vacuum and sent to SOLEIL. This is too high risk, and is the primary motivation for this project to develop the characterization ability in-house.

In this chapter the existing techniques are introduced.

7.1 Diffractometer

With the knowledge that we are interested in measuring angles θ_i and θ_d, the obvious path is to construct an instrument around two ultra-precise goniometers, one to measure each angle. The coherent plane wave to illuminate the diffraction grating with simply requires a near monochromatic light source such as a HeNe laser, expanded to larger than the pattern area. This is the

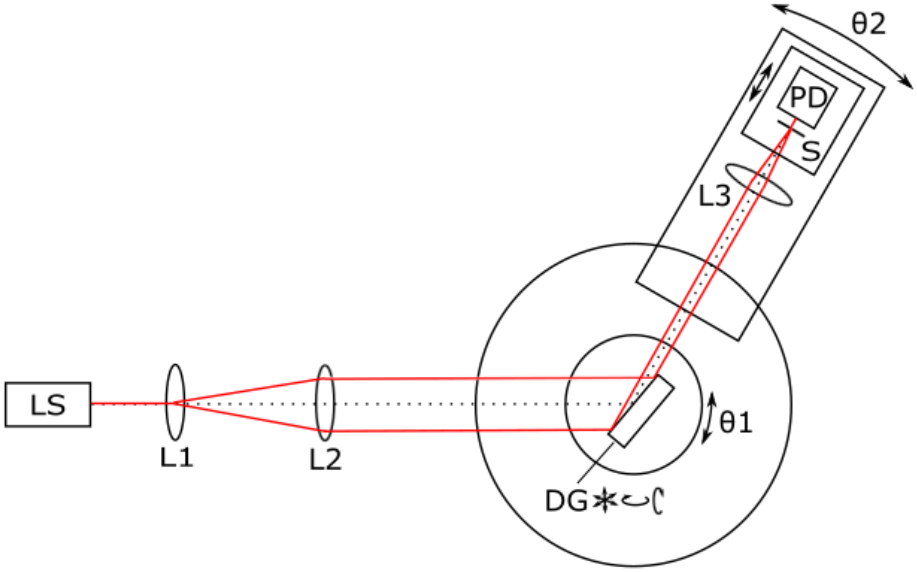

Figure 7.1: Schematic of a diffractometer. The diffraction grating DG is mounted on a stage with all six translational and rotational degrees of freedom. The angular width of the diffracted beam is scanned by a rotating arm with a focusing lens, exit slit, and photodiode.

diffractometer, the schematic for which is given in Figure 7.1.

This works well for constant line spacing diffraction gratings where there is no need for spatial resolution in the x dimension (along the diffraction grating pattern). The geometries involved makes it difficult to motorize the required translational degree of freedom while keeping the point of diffraction on axis such that the angles are measured correctly. This makes the diffractometer unsuitable for not only VLS gratings, but also simply poor quality constant line spacing ones where localized error, as typical of those of mechanical origin, is present.

The vast majority of X-ray optics the metrology teams at synchrotron facilities characterize are mirrors, flat and curved. Decades of development in mirror metrology has built up a wealth of infrastructure and expertise within the US National Lab system. It is clear that diffraction gratings are more complex than mirrors, but fortunately under some conditions they can be reduced to mirrors. Then the problem would be reduced to repurposing existing tools, as opposed to inventing new.

7.2 The Littrow Condition

Referring back to Equation 6.1, we see that for at least the cases of m = 0 and m = ±1 there exist θ_i such that $\theta_d = \theta_i$. It is assumed here that $\frac{\lambda}{d} < 2$, as otherwise diffraction would not happen at all. We have then:

$$2dsin(\theta_{L,m}) = m\lambda \tag{7.1}$$

where $\theta_{L,m} = \theta_i = \theta_d$ denotes the mth order Littrow angle, the angle of incidence at which the mth order diffracted beam returns along the incidence path. At these angles diffraction gratings behaves like a conventional mirror seen at normal incidence, only with significantly lower reflectivity.

As before, to generalize to the VLS case d comes a function of x, and so does $\theta_{L,m}$.

7.3 The Long Trace Profiler

The Long Trace Profiler (LTP) is a slope error measuring instrument developed specifically for characterizing the large mirrors used in synchrotrons and also in space applications, with sub-microradian angular resolution. The general principle is simple: a light source reflects off the surface under test (SUT) and small angular deflections in the return beam is imaged by a lens onto a photodetector, whereby it becomes a translation across the detector. Use of high quality, low aberration optics and careful alignment allows the angle to translation calibration to be linear over angular range of a degree (≈0.02 radians). Furthermore, they are built with ultra-stable translation stages to enable the instrument to scan the beam across mirrors as long as one meter or more in length. Extraordinary efforts were made to optimize linearity in the translation stage. It is mounted on a 12,000 kilogram granite gantry, with the cables from the electronics mounted onto the scanning head carried over to a secondary parallel translation stage with its own gantry, just to carry the cables so as to minimize drag forces on the main translation.

The LTP at Argonne's Advance Photon Source had undergone multiple improvements since the original design by Peter Takacs of Brookhaven National Laboratory [45, 46, 47], to recently demonstrated 50nrad resolution by the current generation system, referred to as an Optical Slope Measurement

System (APS-OSMS)[48].

A perfect diffraction grating ruled to the correct d(x) specifications and therefore correct θ_L(x) specifications will act like a flat mirror at the local Littrow angle – there will be zero deflection in the return beam. Conversely, any resolved deflection implies error in θ_L(x), with the deflection being a measurement of $\Delta\theta = \theta_d$ - θ_i. Since θ_i is set and therefore measurable, this would hypothetically provide enough information for d(x) to be derived. The only remaining issue then is the significantly lower return beam intensity from diffraction gratings optimized for X-rays compared to mirrors. This necessitated an upgrade of the light source to a much brighter 20mW HeNe laser, a joint investment between Argonne and BNL optics groups. For photographs of the APS-OSMS refer to Figure 8.4.

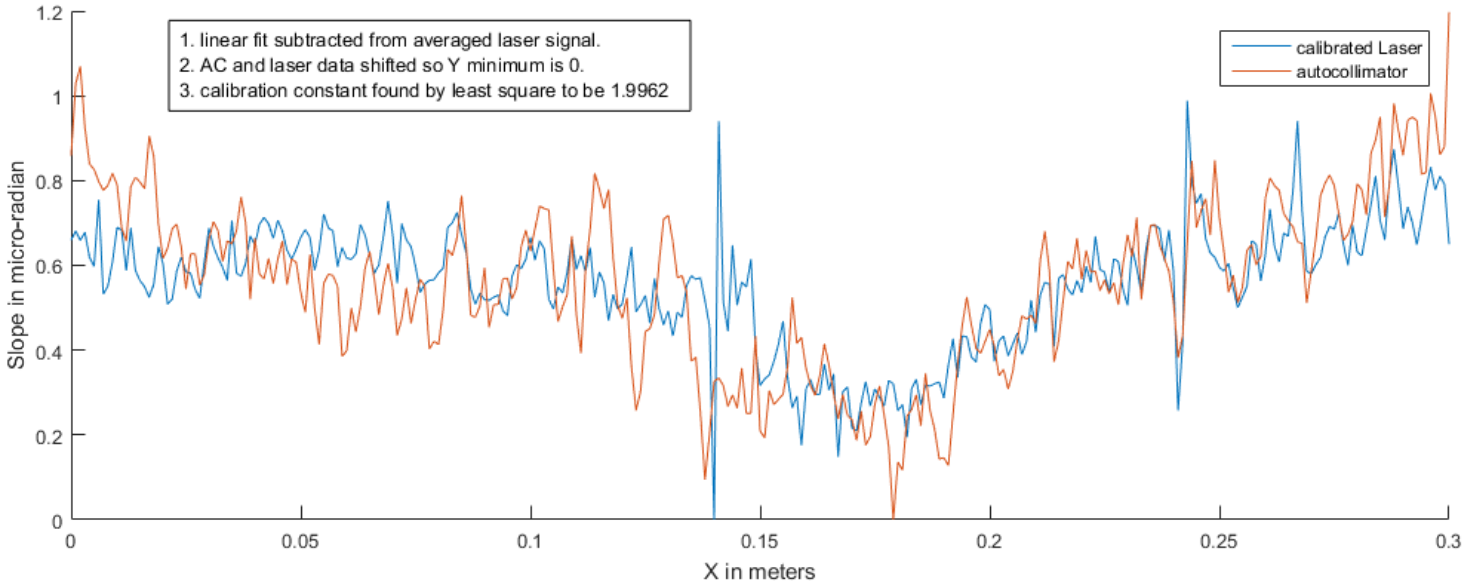

Figure 7.2: Example calibration of the OSMS at Argonne, using an ultra flat mirror as test sample. In this case instead of calibrating against an LTP at a different facility, the new laser excitation path is compared against the old, previously calibrated, path.

Calibrations already exist for the instrument, done by a mirror round robin, where the synchrotron facilities take turns scanning one or two designated standard mirrors and essentially calibrate their instruments against each other. Conveniently at Argonne the instrument was designed with an eye towards future modifications, with enough space to accommodate the new laser path without interfering with the functionality of the previous path. Thus, we have an instrument to calibrate against not just in-house, but sharing mostly the same structural and environmental variables. An example calibration is seen in Figure 7.2.

CHAPTER 8

DEVELOPMENT OF THE APS-OSMS FOR METROLOGY ON VLS DIFFRACTION GRATINGS

8.1 Adding Needed Degrees of Freedom

The first necessary addition to the APS-OSMS is the ability to set the angle of incidence θ_i to values very far from the normal incidence (corresponding to θ_i) all LTPs are designed to operate at. Clearly one can tilt the beam with two additional mirrors or tilt the substrate with an additional tilt platform to change θ_i. In this context the primary concern is in how the additions will contribute to system error.

Using a diffraction grating with constant line density of 2500 grooves per millimeter (gpmm) as test sample, test scans were performed in both configurations in a variety of x translation step sizes. A comparison between beam tilt versus substrate tilt configuration with step size 0.1mm is shown in Figure 8.2. While the large features on the order of ten pixels overlap very well, it is immediately clear that the substrate tilt configuration suffers in spatial resolution, because it is really scanning a compressed projection of the x axis. To end up with the same spatial resolution compared to the beam tilt configuration, one would need to use about half the step size in substrate tilt configuration given this Littrow angle of 52.3°, which in turn would increase the error contribution from the translation stage.

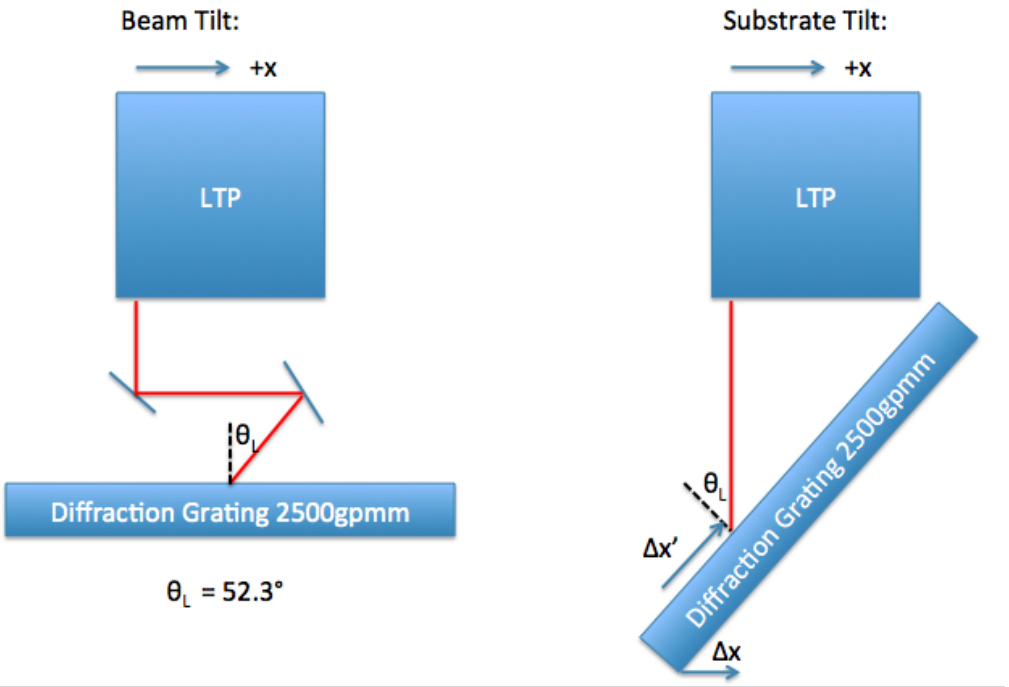

Figure 8.1: Schematic of the two first test prototypes. Of particular importance is that in the substrate tilt case the instrument's x translation axis is no longer aligned with the x axis to be scanned across.

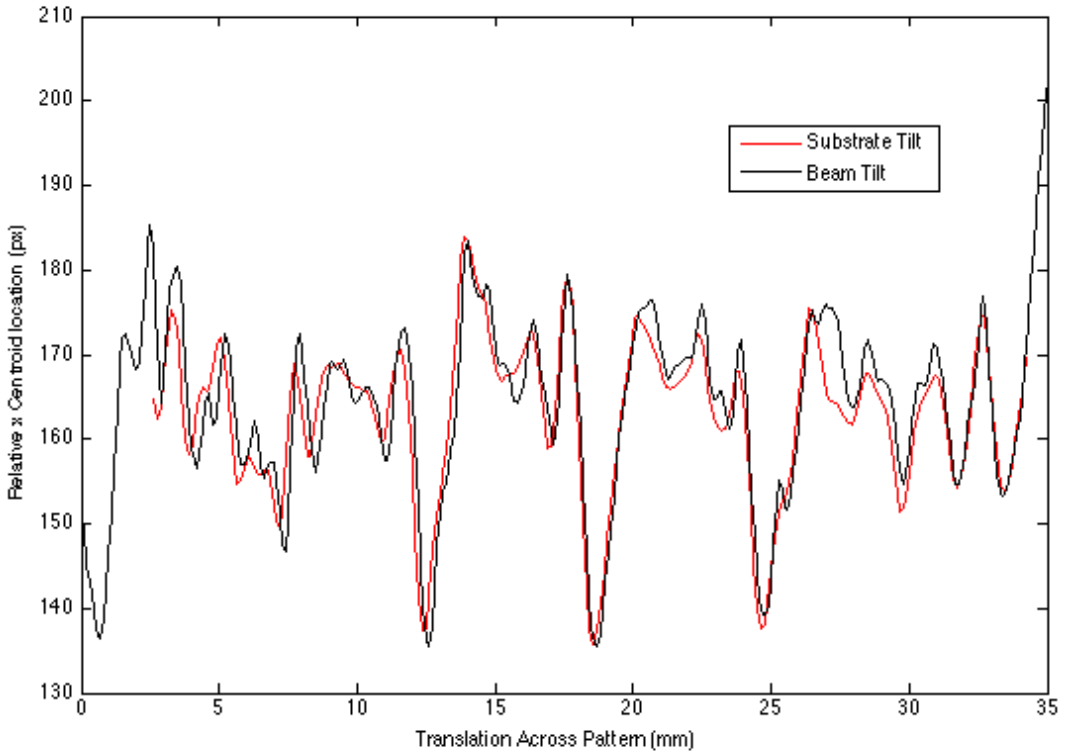

Figure 8.2: Overlay of scans across the midline of a 2500 gpmm diffraction grating. Ignoring the higher spatial frequencies only present in the black line (beam tilt), the agreement is within the errors we expected for the crude optomechanics we used in the prototype.

It is also noted that in the substrate tilt configuration the weight of the diffraction grating will fall on one side of the rectangular substrate, as opposed to evenly distributed across its bottom, the orientation in which its flatness was certified and in which the grooves of the diffraction grating were ruled. Additionally, communication with the metrology team at SOLEIL, the synchrotron facility near Paris, revealed that they decided to tilt the beam after performing their own tests. For these reasons we proceed with the beam tilt strategy and move on to design work for permanent mounting of the two mirrors and rotation stage.

The challenge with performing metrology on diffraction gratings come from the fact that they have many degrees of freedom, and are very much three dimensional. Incorrectly aligning the test sample with the axes of the instrument, whether due to the lack of a good procedure or due to insufficient adjustments, can easily lead to measuring the wrong angles. Alternatively, misalignment can also mean that the diffracted beams are not found at the angles they are expected to be, and in cases where diffraction efficiency is low they are not visible by eye. In Figure 8.3 the vectors are identified and defined for clarity.

Argonne staff engineer Sunil Bean performed the drafting and optimization work in the custom frames once the technical requirements on angular resolution, stability, and range were identified. The design objective is two-fold. First, the first mirror (M1 in Figure 8.3) is mounted on a sliding platform with multiple alignment pins, such that it can be out of the way so the OSMS can be used without the modifications when desired, without compromising alignment on the added parts. Second, as everything will be added onto the gantry-mounted translation platform, all frames were cut down to the bare minimum required for stability so as not to add unnecessary weight, which would degrade the performance of the translation.

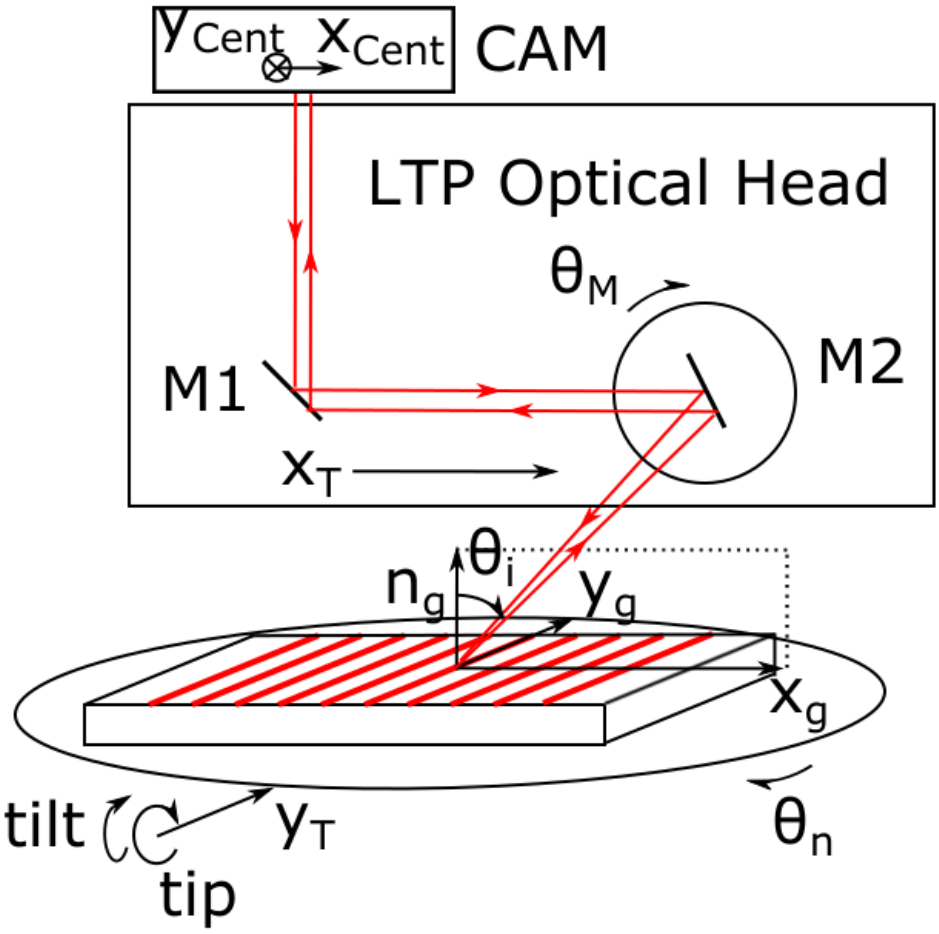

Figure 8.3: The degrees of freedom involved in metrology of diffraction gratings. In particular, given that grooves are parallel, they define a direction y_g which is the normal to the plane in which all diffracted orders lie. When this plane is aligned to the camera's x_{Cent} axis, $\Delta\theta = \theta_d$ - θ_i is proportional to Δx_{Cent} by a calibration constant which could be empirically determined.

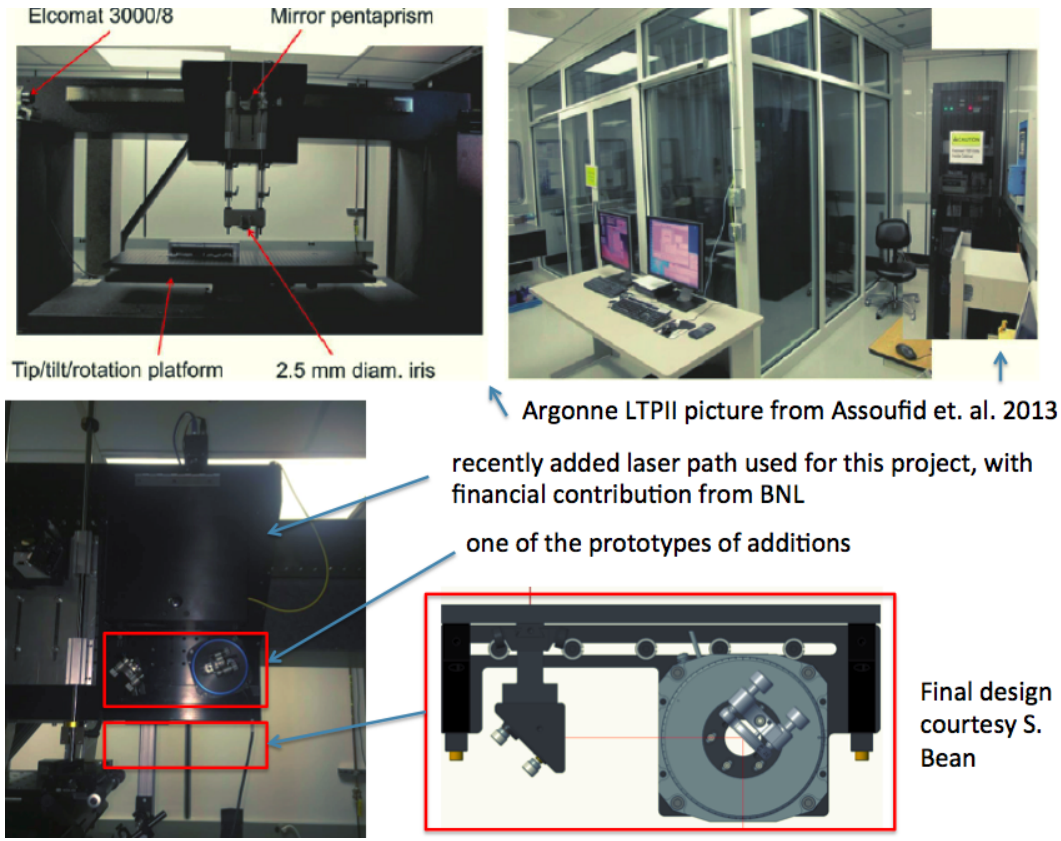

Figure 8.4: Long Trace Profiler (APS-OSMS) at the Advanced Photon Source at Argonne National Laboratory. **Upper Left**: The APS-OSMS before additions, showing only the autocollimator path. Picture from [48]. **Upper Right**: Environmental enclosure of the APS-OSMS which is inside a class 10,000 clean room. Picture from [48]. **Lower Left**: Close up of scanning head showing laser path (black enclosure) and prototype additions. Final addition to be added in area indicated by red box. **Lower Right**: Final design courtesy Sunil Bean.

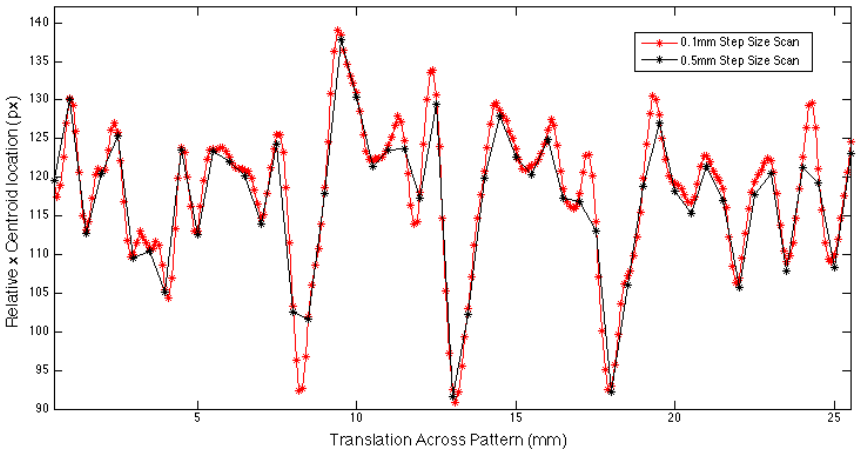

Figure 8.5: Overlay of scan at 0.5mm step size versus 0.1mm step size.

Of particular importance is the addition of a 360° piezo rotation stage to supplement the mirror mount which has only 4° range per adjuster, insufficient to adjust for all possible Littrow angles. The fact that it is motorized allows the incident angle to be precisely read out relative to the surface normal, as will be discussed next section. This turns what was a relative measurement with the prototype setup (need to assume $\theta_d = \theta_L$ at x = 0) to an absolute measurement, as depicted in the inset to Figure 8.8.

8.2 Scan Step-size Comparison

The spatial resolution achievable by the instrument depends on multiple variables, an important one of which is the effective spot size of the illumination beam on the surface. The nominal beam diameter out of the fiber is about 1mm. This will be sheared as the cosine of the angle of incidence, with the width stretched by a factor of three at $\theta_L = 70.5°$ which corresponds to, given that for the OSMS $\lambda = 632.8$nm, a d of $\frac{3}{2}\lambda = 949.2$nm at first order. It is reasonable to expect d to vary from 400nm up to 2000nm (corresponding to line densities 500gpmm up to 2500gpmm), so this effective widening of the incident beam must be taken into account in optimizing scan step size versus how long each scan takes. At scan times of hours versus minutes, environmental drift effects such as those caused by temperature fluctuations start to become measurable in magnitude (order of 10nrad).

A test comparing a scan at 0.1mm step size versus 0.5mm step size, where the effective beam width was about 1.6mm. The hypothesis was that 0.1mm would be too small a step size given the width, and essentially it would not yield more information than the 0.5mm step size scan. However as seen in Figure 8.5 it matched all 0.5mm points where both were sampled, with the 0.1mm scan step trace seeing distinct peaks and valleys between steps in the 0.5mm trace. The good agreement between the traces suggest that drift effects are minimal. Also, recalling the fact that the diffraction grating scanned for this test had line density 2500gpmm, what this data means is that sliding an illumination window of $1.6mm \times 2500\frac{grooves}{mm} = 4000$ grooves a step of $0.1\text{mm} \times 2500\frac{grooves}{mm} = 250$ grooves leads to a resolvable difference in θ_d, which will depend on the quality of the diffraction grating in question.

This is in contrast to the metrology of X-ray mirrors usually performed on the LTP, where step sizes of 1mm or larger are routinely employed. Mirrors, which are made by incremental polishing to form the surface figure, simply do not tend to have errors with high spatial frequency.

8.3 Improved Angle Calibration Using Piezo Rotation Stage

Addition of the motorized rotation stage makes possible a somewhat obvious way to calibrate the angle per pixel constant across the full field of the camera. The second mirror (M2, which is mounted on the rotation stage) could be used as the test mirror. It only needs to be rotated via the stage such that the incident beam from M1 arrives at normal incidence. Then the stage could be stepped to tilt the mirror surface incrementally, scanning the reflected beam across the camera's field. In essence this is a calibration of the linearity of the Fourier lens system against that of the rotation stage. This scan is plotted in Figure 8.6.

In making use of this calibration, it is important to keep in mind that the change in angle of tilt of the mirror surface is not the same the change in angle of the surface normals – there is a factor of two. This is a critical point and is illustrated in Figure 8.7. As what we are measuring for diffraction gratings, $\Delta\theta = \theta_d$ - θ_i is actually equal to the angular change of the surface normals, which is double the angle the calibration constant $3.47\frac{\mu rad}{px}$ was derived from,

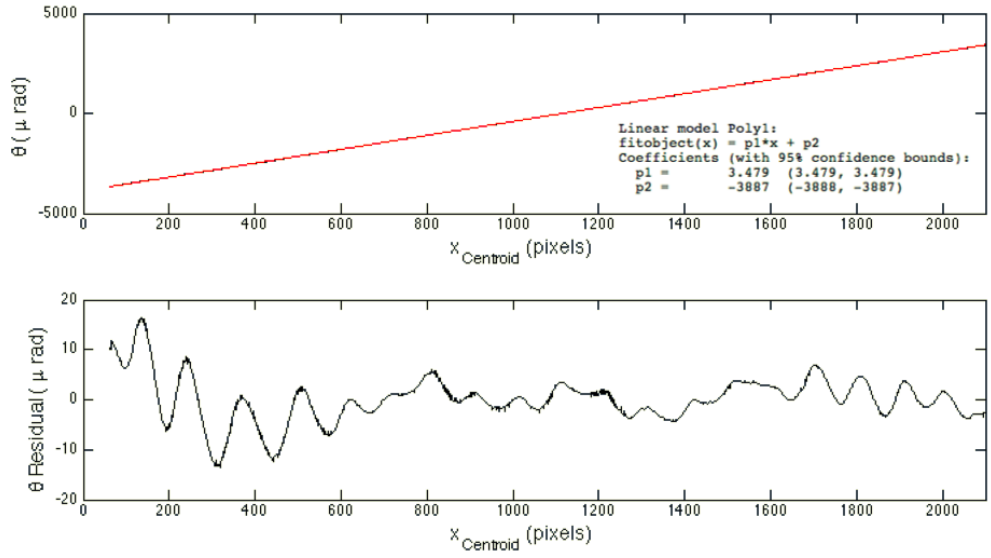

Figure 8.6: Results of calibration done using the piezo rotation stage. Top: As the mirror is tilted the response on camera is extremely linear, across central 2100 pixels of the 2444 pixel wide field. Bottom: Residuals of linear fit with angle to pixel constant $3.47\frac{\mu rad}{px}$.

we need to double the constant and use instead $6.94\frac{\mu rad}{px}$.

8.4 Characterization of VLS Coefficients of IEX Beamline Diffraction Grating

8.4.1 Single Screen Scan

A VLS diffraction grating previously characterized by SOLEIL is currently not in use in its intended Argonne beamline IEX, and is an obvious first test for the new system. The strategy used was, referring to the labels in Figure 8.3:

1. First use translations x_T and y_T to locate the edges of the substrate and align rotation θ_n.

2. At center of the diffraction grating pattern, establish θ_M axis value corresponding to surface normal n_g, which we will refer to as θ_v.

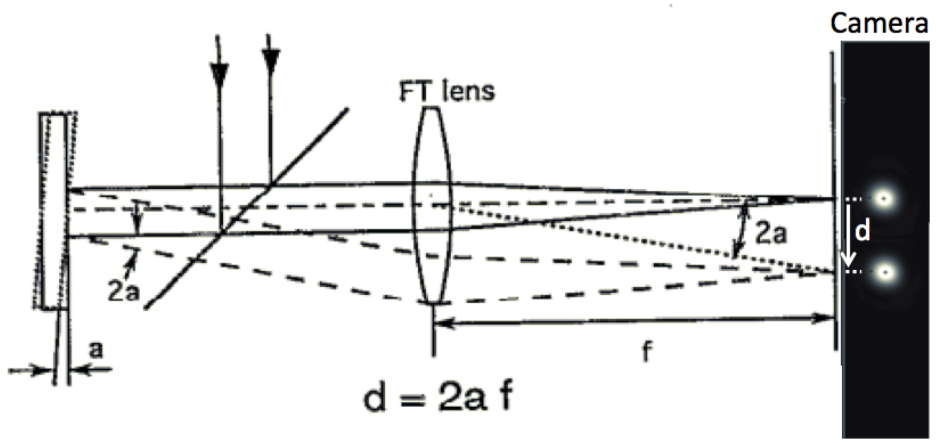

Figure 8.7: LTP measures angle $\delta\theta$ as translation of image of return beam on the camera, here denoted by d. The Law of Reflection allows the angle between incident and return beam, 2a here, to be related to the angular tilt of the substrate, a, in the case of the test surface being a mirror. Figure modified from [45]

3. Using θ_M and x_T in combination, set incidence angle $\theta_i = \theta_L = 2 \times(\theta_M - \theta_v)$ at the center of the diffraction grating, using the specifications as a guide. It may require some searching to get the return beam on camera. Iterate to center return beam in x_{Cent}. In this case θ_M was set to 57.0340°, corresponding to incident angle 22.3284°. The theoretical Littrow angle was 22.3213°.

4. Adjust tilt to center return beam in y_{Cent}.

5. Translate x_T across full length of pattern to make sure return beam scans across a straight horizontal line on camera, such that $\Delta\theta$ is entirely along x_{Cent}. In this case the scan spanned the central 1820 pixels of the camera. The theoretical calculations from manufacturer specifications are presented in Figure 8.8.

6. Perform scan. The scan result is presented in Figure 8.9.

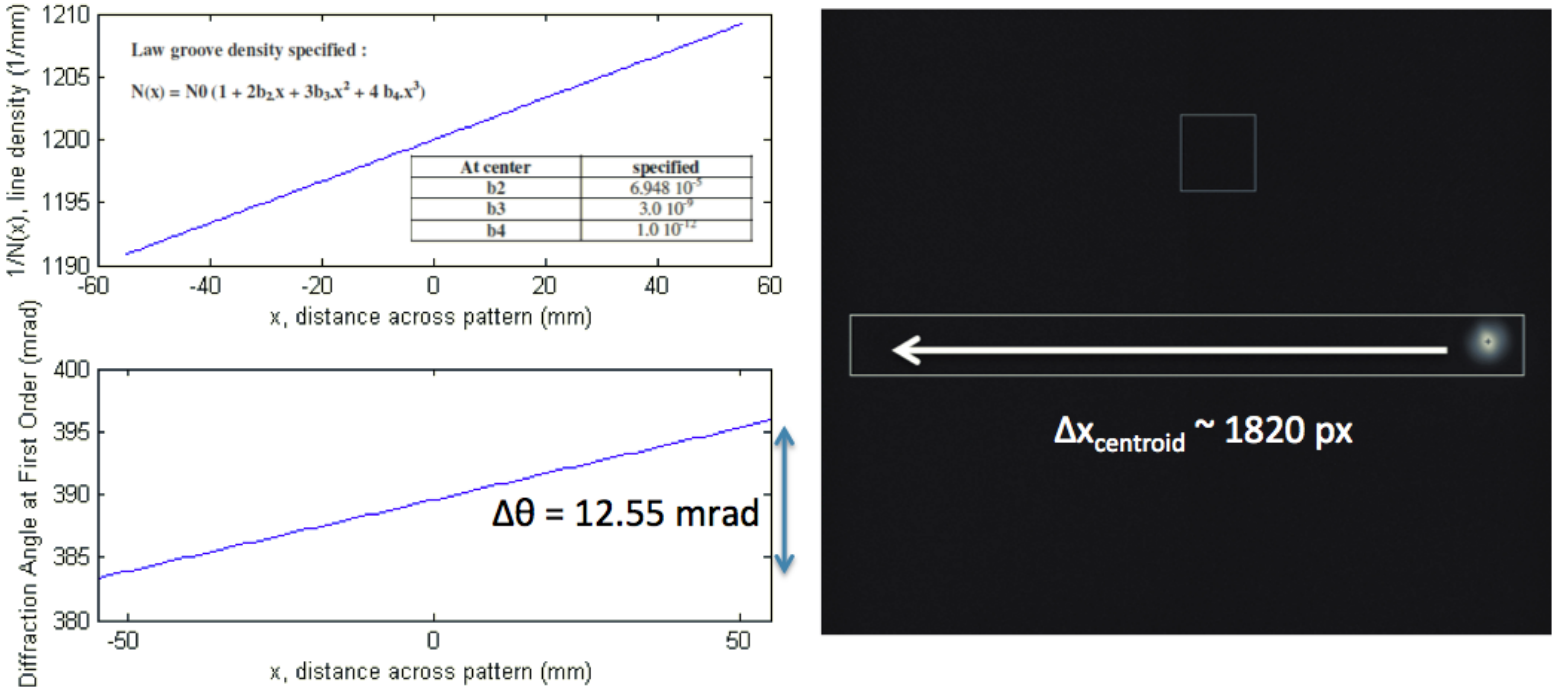

Figure 8.8: Calculations for the IEX VLS grating using specifications from manufacturer Horiba. Upper Left: Location line density as a function of distance across pattern. Lower Left: First order diffraction angle θ_d defection relative to value at center of diffraction grating, showing total deflection range of 12.55mrad. Right: According to the camera calibration this angular range corresponds to approximately 1800 pixels.

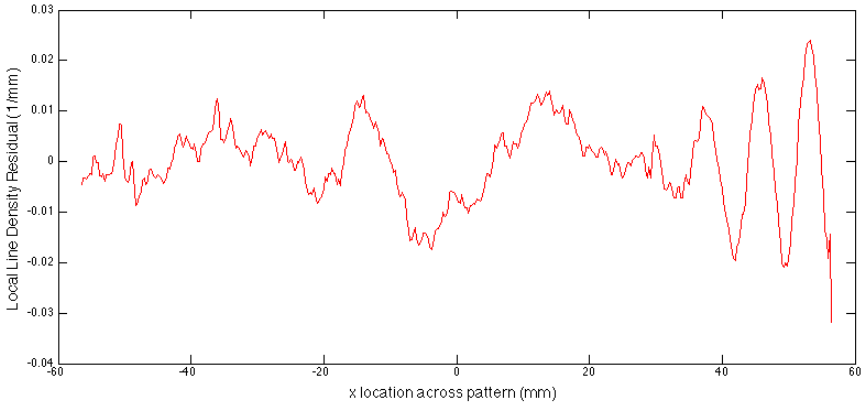

Figure 8.9: Residual of local line density derived from scan, after fit to third order polynomial of the form $N_0 \times (1 + 2b_2x + 3b_3x^2 + 4b_4x^3)$. The coefficients are listed in Table 8.1.

The APS-OSMS coefficients agree with those from SOLEIL very well. From our scan we would have concluded that the diffraction grating was manufactured to specifications, the same conclusion reached by the metrology team at SOLEIL.

8.5 Conclusion and Future Work

Now that the APS-OSMS has successfully reproduced a VLS diffraction grating scan result, the next steps are to prepare for the first real samples, further error mitigation, and development of standard protocols for its function as a user facility.

Table 8.1: VLS Coefficients of IEX Grating

	Specs	**APS-OSMS**	**SOLEIL**
N_0	1200	1199.22	1200.9954
b_2	6.948×10^{-5}	6.8996×10^{-5}	7.046×10^{-5}
b_3	3.0×10^{-9}	3.6604×10^{-9}	4.2×10^{-10}
b_4	1.0×10^{-12}	3.063×10^{-11}	1.98×10^{-11}

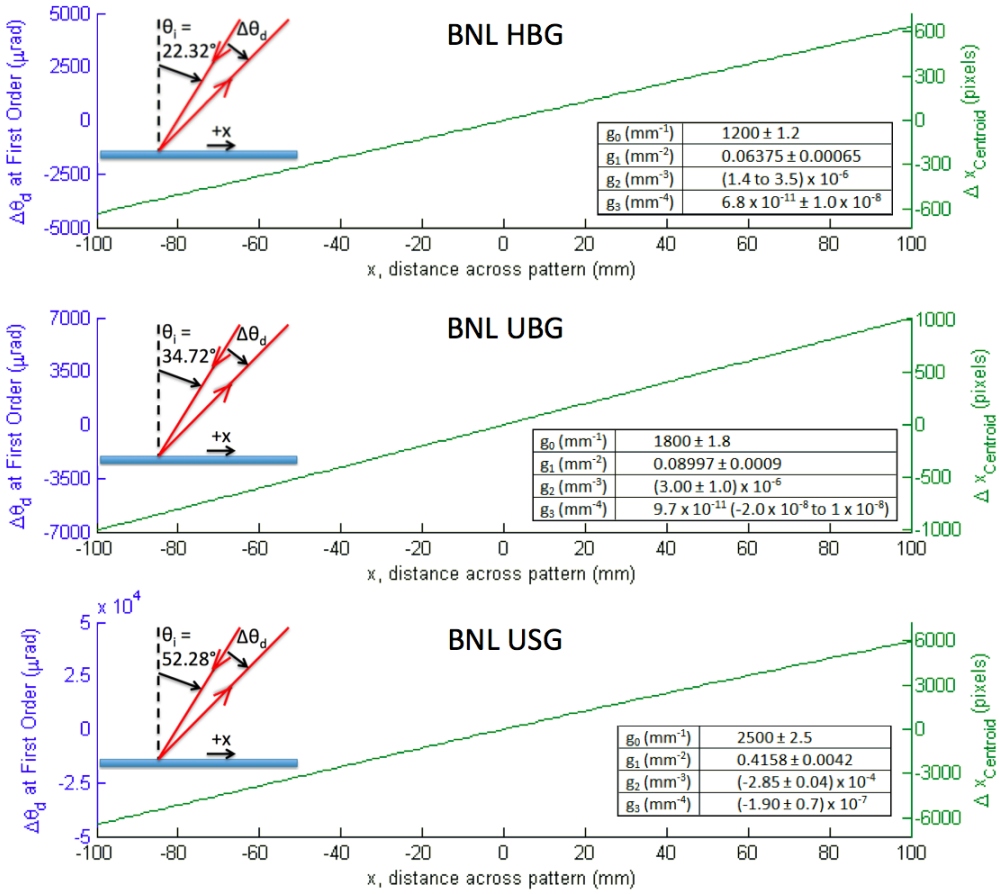

Figure 8.10: Predicted θ_d curves for the three BNL diffraction gratings to be characterized at APS-OSMS in December 2016.

8.5.1 First Real Metrology Work – BNL VLS Gratings

The three BNL VLS diffraction gratings the Argonne-APS metrology team will characterize are either completed or being ruled as of this writing (November 2016). The specifications are already known, and based on that information the predicted $\Delta\theta_d$ curves as functions of x are plotted in Figure 8.10. The APS-OSMS has camera width 2444 pixels, of which the central 2100 pixels were calibrated. It is immediately clear that for the third diffraction grating, USG, θ_d deflects through enough range to require at least five full camera widths, and that is without allowing overlap in the scans for stitching.

Not just for the USG diffraction grating, but in general, a stitching algorithm must be developed for the APS-OSMS to be able to handle aggressive

VLS laws.

8.5.2 Multi-Screen Scan

To acquire test data for development of the stitching algorithm, the IEX diffraction grating is intentionally re-scanned using a fraction of the camera, with large overlaps. Figure 8.11 shows the eleven resulting scans, each centered ten millimeters apart on the diffraction grating, so each was taken at a different θ_i to recenter the return beam on the camera. Each scan includes twenty millimeters of overlap on each side for stitching.

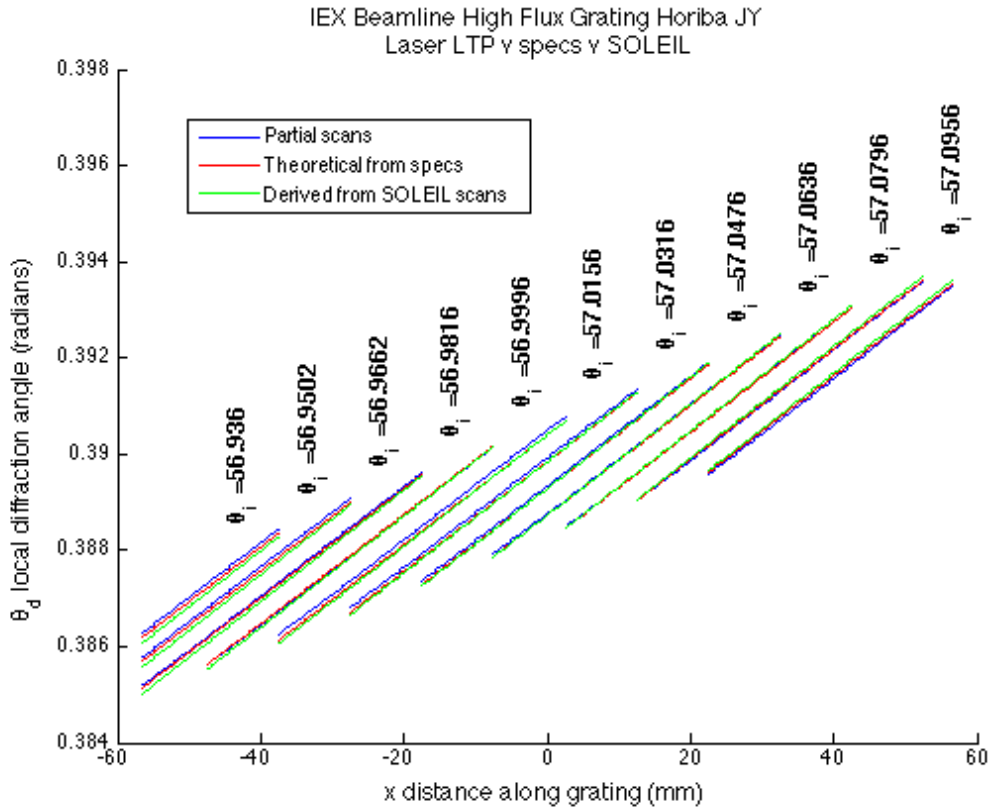

Figure 8.11: IEX VLS diffraction grating intentionally scanned over eleven different traces for stitching test.

The θ_d scans can be converted into d(x) using the diffraction grating equation (Equation 6.1). The resulting curves already align very well with each other, though the match is not perfect and a simple average would not suffice (Figure 8.12).

The algorithm to combine these curves is currently under development, and the single screen scan of the same diffraction grating presented in Section 8.4.1 will be used for comparison to minimum distortion caused by stitching.

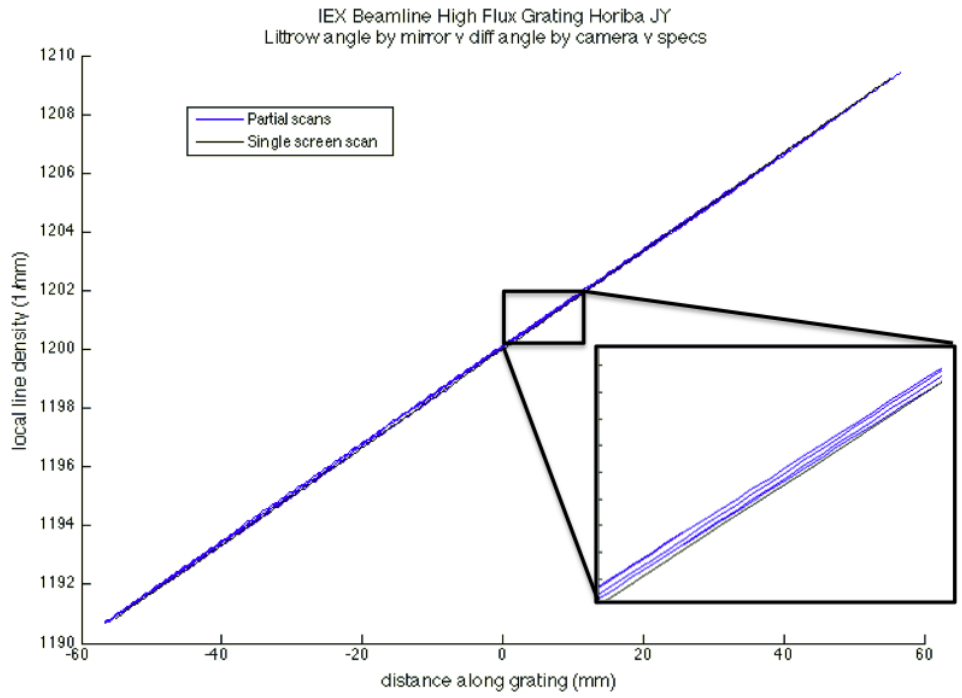

Figure 8.12: Multi-screen test scan of IEX diffraction grating, plotted is d as a function of x.

APPENDIX A

APPENDIX – MATLAB CODE

```
%% DATA VARIATION CHECK
% LOAD all FCS files
clear t_all G_all
numtraces = 5;
fileprefix = '';
for i = 1:numtraces
    filename = [fileprefix num2str(i) '.txt'];
    delimiterIn = '\t';
    headerlinesIn = 1;
    A = importdata(filename,delimiterIn,headerlinesIn);
    t_all{i} = A.data(:,1).*10^-3; \% CONVERT TO SECONDS
    G_all{i} = A.data(:,2);
end
\%\% Select Data Subset
t_low = 1*10^-6; % 1 microsecond lowerbound
t_high = 1; % one second upperbound
goodpts = t_all{1}> t_low & t_all{1}<t_high;
for i = 1:numtraces
    t_all{i} = t_all{i}(goodpts);
    G_all{i} = G_all{i}(goodpts);
end
% PLOT
figure(1);
semilogx(t_all{1},G_all{1},'-');
hold on
for i = 2:numtraces
semilogx(t_all{i},G_all{i},'-');
end
```

```
hold off
xlabel('Time (s)')
ylabel('G(t)')
%title(['Coherent 637nm laser Alexa-GBP 3 trace tetraspeck check'])
print('data variation check', '-dpng')
%% FITTING PARAMETERS

% initialize arrays
Parameters.tauT = zeros(numtraces,1);
Parameters.tauD = zeros(numtraces,1);
Parameters.N = zeros(numtraces,1);
Parameters.T = zeros(numtraces,1);
Parameters.K = zeros(numtraces,1);
% boundary conditions
tauT_L = 1e-8;
tauT_H = 1e-4;
N_L = 0.1;
N_H = 100;
tauD_L = 1e-5;
tauD_H = 1e-3;
T_L = 0.1;
T_H = 0.8;
%K_L = 2;
%K_H = 6;
K_L = 1;
K_H = 10;

%% FITTING LOOP
% Initial T and K
T = 0.4;
K = 4;
% Initial guesses
tauT = 1e-7; % one microsecond
tauD = 1e-4; % one hundred microseconds
N = 1;
% fit options
```

```
options = optimoptions(@lsqcurvefit,'MaxIter',...
    1500,'MaxFunEvals',10000,'TolFun',1e-12);

for i = 1:numtraces
    t = t_all{i};
    G = G_all{i};

% fit function 1
% 1st function (T and K held constant); [tauT N tauD]
T_and_K_const = @(a,t)(1-T+T.*exp(-t./a(1))).*(1/a(2)).*...
    (1./(1+t./a(3))).*(1./(1+t./(K^2*a(3))).^0.5)+1;
% fit 1
[a1,resnorm,residual,exitflag,output] = lsqcurvefit(T_and_K_const,...
    [tauT N tauD],t,G,[tauT_L N_L tauD_L],[tauT_H N_H tauD_H],options);
disp(['exitflag = ' num2str(exitflag)])
disp(['tauT = ' num2str(a1(1))])
disp(['N = ' num2str(a1(2))])
disp(['tauD = ' num2str(a1(3))])
disp(['Residual Sum of Squares = ' num2str(sum(resnorm))])
% PLOT output
figure(1);
semilogx(t,G,'-');
hold on
Gout = T_and_K_const(a1,t);
semilogx(t,Gout,'-k','LineWidth',2);
hold off
xlabel('Time (s)')
ylabel('G(t)')
title(['Fit 1 result, Residual Sum of Squares = ' num2str(sum(resnorm))])
%print(['Trace #' num2str(i) ' Fit 1'], '-dpng')
% Fit 2
% 2nd function (output of 1st function held constant); [T K]
Taus_and_N_const = @(a,t)(1-a(1)+a(1).*exp(-t./a1(1))).*(1/a1(2)).*...
    (1./(1+t./a1(3))).*(1./(1+t./(a(2)^2*a1(3))).^0.5)+1;
% fit
[a2,resnorm,residual,exitflag,output] = lsqcurvefit(Taus_and_N_const,...
```

```
    [T K],t,G,[T_L K_L],[T_H K_H],options);
disp(['exitflag = ' num2str(exitflag)])
disp(['T = ' num2str(a2(1))])
disp(['K = ' num2str(a2(2))])
disp(['Residual Sum of Squares = ' num2str(sum(resnorm))])
% PLOT output
figure(2);
semilogx(t,G,'-');
hold on
Gout = Taus_and_N_const(a2,t);
semilogx(t,Gout,'-k','LineWidth',2);
hold off
xlabel('Time (s)')
ylabel('G(t)')
title(['Fit 2 result, Residual Sum of Squares = ' num2str(sum(resnorm))])
%print(['Trace #' num2str(i) ' Fit 2'], '-dpng')
% Fit 3
% 3rd function (output of 1st and 2nd function used as initial); [a1 a2]
% [tauT N tauD T K]
All_free = @(a,t)(1-a(4)+a(4).*exp(-t./a(1))).*(1/a(2)).*...
    (1./(1+t./a(3))).*(1./(1+t./(a(5)^2*a(3))).^0.5)+1;
% fit
[a3,resnorm,residual,exitflag,output] = lsqcurvefit(All_free,...
    [a1 a2],t,G,[tauT_L N_L tauD_L T_L K_L],...
    [tauT_H N_H tauD_H T_H K_H],options);
% [tauT N tauD T K]
disp(['exitflag = ' num2str(exitflag)])
disp(['tauT = ' num2str(a3(1))])
disp(['N = ' num2str(a3(2))])
disp(['tauD = ' num2str(a3(3))])
disp(['T = ' num2str(a3(4))])
disp(['K = ' num2str(a3(5))])
disp(['Residual Sum of Squares = ' num2str(sum(resnorm))])
% PLOT output
figure(3);
semilogx(t,G,'-');
```

```
hold on
Gout = All_free(a3,t);
Gfit{i} = All_free(a3,t);
semilogx(t,Gout,'-k','LineWidth',2);
hold off
xlabel('Time (s)')
ylabel('G(t)')
title(['Fit 3 result, Residual Sum of Squares = ' num2str(sum(resnorm))])
%
    a = axis;
    wdth = a(2)-a(1);
    ht = a(4)-a(3);
    pos = [a(1)+0.015*wdth a(4)-0.15*ht];
    h = text(pos(1),pos(2),{['tauT = ' num2str(a3(1)) 's'];
['N = ' num2str(a3(2))];
['tauD = ' num2str(a3(3)) 's'];
['T = ' num2str(a3(4))];
['K = ' num2str(a3(5))]});
%
print(['Trace #' num2str(i) ' Fit 3'], '-dpng')
% residuals plot
figure(4);
semilogx(t,residual,'-');
xlabel('Time (s)')
ylabel('G(t)')
title('Fit 3 Residuals')
print(['Trace #' num2str(i) ' Fit 3 Residuals'], '-dpng')
% save outputs
Parameters.tauT(i) = a3(1);
Parameters.N(i) = a3(2);
Parameters.tauD(i) = a3(3);
Parameters.T(i) = a3(4);
Parameters.K(i) = a3(5);
end
save('Parameters.mat','Parameters');
disp('Average tauD')
```

```
mean(Parameters.tauD)
disp('+/- (stdev)')
std(Parameters.tauD)
%% Fitting Loop
% initialize arrays
Parameters.tauD = zeros(numtraces,1);
Parameters.N = zeros(numtraces,1);
Parameters.K = zeros(numtraces,1);
% Boundary Conditions
N_L = 0.01;
N_H = 1000;
tauD_L = 1e-6;
tauD_H = 1e-1;
K_L = 2;
K_H = 6;

% Initial K
K = 3;
% Initial guesses
tauD = 1e-3; % one millisecond
N = 1;
% fit options
options = optimoptions(@lsqcurvefit,'MaxIter',...
    1500,'MaxFunEvals',10000,'TolFun',1e-12);

for i = 1:numtraces
    t = t_all{i};
    G = G_all{i};
% fit function 1
% 1st function (K held constant); [N tauD]
K_const = @(a,t)(1/a(1)).*(1./(1+t./a(2))).*...
    (1./(1+t./(K^2*a(2))).^0.5)+1;
% fit 1
[a1,resnorm,~,exitflag,~] = lsqcurvefit(K_const,...
    [N tauD],t,G,[N_L tauD_L],[N_H tauD_H],options);
disp(['exitflag = ' num2str(exitflag)])
```

```
disp(['N = ' num2str(a1(1))])
disp(['tauD = ' num2str(a1(2))])
disp(['Residual Sum of Squares = ' num2str(sum(resnorm))])
% PLOT output
figure(1);
semilogx(t,G,'-');
hold on
Gout = K_const(a1,t);
semilogx(t,Gout,'-k','LineWidth',2);
hold off
xlabel('Time (s)')
ylabel('G(t)')
title(['Fit 1 result, Residual Sum of Squares = ' num2str(sum(resnorm))])
%print(['Trace #' num2str(i) ' Fit 1'], '-dpng')
% Fit 2
% 2nd function (output of 1st function held constant); [K]
Tau_and_N_const = @(a,t)(1/a1(1)).*(1./(1+t./a1(2))).*...
    (1./(1+t./(a(1)^2*a1(2))).^0.5)+1;
% fit
[a2,resnorm,residual,exitflag,output] = lsqcurvefit(Tau_and_N_const,...
    [K],t,G,[K_L],[K_H],options);
disp(['exitflag = ' num2str(exitflag)])
disp(['K = ' num2str(a2(1))])
disp(['Residual Sum of Squares = ' num2str(sum(resnorm))])
% PLOT output
figure(2);
semilogx(t,G,'-');
hold on
Gout = Tau_and_N_const(a2,t);
semilogx(t,Gout,'-k','LineWidth',2);
hold off
xlabel('Time (s)')
ylabel('G(t)')
title(['Fit 2 result, Residual Sum of Squares = ' num2str(sum(resnorm))])
%print(['Trace #' num2str(i) ' Fit 2'], '-dpng')
% fit 3
```

```
% last function [N tauD K]
D_only_allfree = @(a,t)(1/a(1)).*(1./(1+t./a(2))).*...
    (1./(1+t./(a(3)^2*a(2))).^0.5)+1;
[a3,resnorm,~,exitflag,~] = lsqcurvefit(D_only_allfree,...
    [a1 a2],t,G,[N_L tauD_L K_L],[N_H tauD_H K_H],options);
disp(['exitflag = ' num2str(exitflag)])
disp(['N = ' num2str(a3(1))])
disp(['tauD = ' num2str(a3(2))])
disp(['K = ' num2str(a3(3))])
disp(['Residual Sum of Squares = ' num2str(sum(resnorm))])
% PLOT output
figure(3);
semilogx(t,G,'-');
hold on
Gout = D_only_allfree(a3,t);
semilogx(t,Gout,'-k','LineWidth',2);
hold off
xlabel('Time (s)')
ylabel('G(t)')
title(['Fit 3 result, Residual Sum of Squares = ' num2str(sum(resnorm))])
%
    a = axis;
    wdth = a(2)-a(1);
    ht = a(4)-a(3);
    pos = [a(1)+0.015*wdth a(4)-0.15*ht];
    h = text(pos(1),pos(2),{
['N = ' num2str(a3(1))];
['tauD = ' num2str(a3(2)) 's'];
['K = ' num2str(a3(3))]});
%
print(['Trace #' num2str(i) ' Fit 3'], '-dpng')
% residuals plot
figure(4);
semilogx(t,residual,'-');
xlabel('Time (s)')
ylabel('G(t)'
```

```
title('Fit 3 Residuals')
print(['Trace #' num2str(i) ' Fit 3 Residuals'], '-dpng')
% save outputs
Parameters.N(i) = a3(1);
Parameters.tauD(i) = a3(2);
Parameters.K(i) = a3(3);
end
save('Parameters.mat','Parameters');
disp('Average tauD')
mean(Parameters.tauD)
disp('+/- (stdev)')
std(Parameters.tauD)
%% LATERAL WIDTH
%Diffusion coefficients - Cy5 = 3.6e-10
% r6g = 4.14e-10 (or 2.8 from Andre's reference)
% rh 110 = 4.7e-10
Temp = 23 + 273.15;
D = 4.4e-10*(Temp/298.15)*((8.94e-4)/(2.414e-5*10^(247.8/(Temp-140))));
Parameters.wx = sqrt(4*D*42.7e-6)
save('Parameters.mat','Parameters');
```

REFERENCES

[1] R. E. Thompson, D. R. Larson, and W. W. Webb, "Precise nanometer localization analysis for individual fluorescent probes," *Biophys. Journal*, vol. 82(5), pp. 2775–2783, 2002.

[2] E. Abbe, "Beitrge zur theorie des mikroskops und der mikroskopischen wahrnehmung."

[3] E. Hecht, *Optics*, 4th ed. Reading, MA: Addison-Wesley, 2002.

[4] M. C. DeSantis, S. H. DeCenzo, J.-L. Li, and Y. M. Wang, "Precision analysis for standard deviation measurements of immobile single fluorescent molecule images," *Opt. Express*, vol. 18, no. 7, pp. 6563–6576, Mar 2010. [Online]. Available: http://www.opticsexpress.org/abstract.cfm?URI=oe-18-7-6563

[5] A. Pertsinidis, Y. Zhang, and S. Chu, "Subnanometre single-molecule localization, registration and distance measurements," *Nature*, vol. 466, no. 7306, pp. 647–651, 2010.

[6] M. T. Hoffman, J. Sheung, and P. R. Selvin, "Fluorescence imaging with one nanometer accuracy: in vitro and in vivo studies of molecular motors," *Single Molecule Enzymology: Methods and Protocols*, pp. 33–56, 2011.

[7] A. e. a. Yildiz, "Myosin v walks hand-over-hand: single fluorophore imaging with 1.5-nm localization," *Science*, vol. 300, p. 2061?2065, 2003.

[8] T. M. V. R. D. . S. P. R. Yildiz, A., "Kinesin walks hand-over-hand," *Science*, vol. 303, p. 5658, 2004.

[9] E. Betzig, G. H. Patterson, R. Sougrat, O. W. Lindwasser, S. Olenych, J. S. Bonifacino, M. W. Davidson, J. Lippincott-Schwartz, and H. F. Hess, "Imaging intracellular fluorescent proteins at nanometer resolution," *Science*, vol. 313, no. 5793, pp. 1642–1645, 2006.

[10] M. J. Rust, M. Bates, and X. Zhuang, "Sub-diffraction-limit imaging by stochastic optical reconstruction microscopy (storm)," *Nature methods*, vol. 3, no. 10, pp. 793–796, 2006.

[11] J. E. Berlier, A. Rothe, G. Buller, J. Bradford, D. R. Gray, B. J. Filanoski, W. G. Telford, S. Yue, J. Liu, C.-Y. Cheung et al., "Quantitative comparison of long-wavelength alexa fluor dyes to cy dyes: fluorescence of the dyes and their bioconjugates," *Journal of Histochemistry & Cytochemistry*, vol. 51, no. 12, pp. 1699–1712, 2003.

[12] E. Rusinova, V. Tretyachenko-Ladokhina, O. E. Vele, D. F. Senear, and J. A. Ross, "Alexa and oregon green dyes as fluorescence anisotropy probes for measuring protein–protein and protein–nucleic acid interactions," *Analytical biochemistry*, vol. 308, no. 1, pp. 18–25, 2002.

[13] V. N. Mochalin, O. Shenderova, D. Ho, and Y. Gogotsi, "The properties and applications of nanodiamonds," *Nature nanotechnology*, vol. 7, no. 1, pp. 11–23, 2012.

[14] A. P. Alivisatos, "Semiconductor clusters, nanocrystals, and quantum dots," *Science*, vol. 271, no. 5251, p. 933, 1996.

[15] M. G. Bawendi, M. L. Steigerwald, and L. E. Brus, "The quantum mechanics of larger semiconductor clusters (" quantum dots")," *Annual Review of Physical Chemistry*, vol. 41, no. 1, pp. 477–496, 1990.

[16] D. Gerion, F. Pinaud, S. C. Williams, W. J. Parak, D. Zanchet, S. Weiss, and A. P. Alivisatos, "Synthesis and properties of biocompatible water-soluble silica-coated cdse/zns semiconductor quantum dots," *The Journal of Physical Chemistry B*, vol. 105, no. 37, pp. 8861–8871, 2001.

[17] A. M. Smith, H. Duan, M. N. Rhyner, G. Ruan, and S. Nie, "A systematic examination of surface coatings on the optical and chemical properties of semiconductor quantum dots," *Physical Chemistry Chemical Physics*, vol. 8, no. 33, pp. 3895–3903, 2006.

[18] E. Cai, P. Ge, S. H. Lee, O. Jeyifous, Y. Wang, Y. Liu, K. M. Wilson, S. J. Lim, M. A. Baird, J. E. Stone et al., "Stable small quantum dots for synaptic receptor tracking on live neurons," *Angewandte Chemie*, vol. 126, no. 46, pp. 12 692–12 696, 2014.

[19] H. S. Choi, W. Liu, P. Misra, E. Tanaka, J. P. Zimmer, B. I. Ipe, M. G. Bawendi, and J. V. Frangioni, "Renal clearance of quantum dots," *Nature biotechnology*, vol. 25, no. 10, pp. 1165–1170, 2007.

[20] N. A. Parris, *Instrumental liquid chromatography: a practical manual on high-performance liquid chromatographic methods*. Elsevier, 2000, vol. 27.

[21] A. Striegel, W. W. Yau, J. J. Kirkland, and D. D. Bly, *Modern size-exclusion liquid chromatography: practice of gel permeation and gel filtration chromatography*. John Wiley & Sons, 2009.

[22] W. Goldburg, "Dynamic light scattering," *American Journal of Physics*, vol. 67, no. 12, pp. 1152–1160, 1999.

[23] *Dynamic light scattering: Common terms defined*, Malvern.

[24] *Intensity - Volume - Number Which Size is Correct?*, Malvern.

[25] *Measuring Quantum Dots Using the Zetasizer Nano*, Malvern.

[26] L. Ma, C. Tu, P. Le, S. Chitoor, S. J. Lim, M. U. Zahid, K. W. Teng, P. Ge, P. R. Selvin, and A. M. Smith, "Multidentate polymer coatings for compact and homogeneous quantum dots with efficient bioconjugation," *Journal of the American Chemical Society*, vol. 138, no. 10, pp. 3382–3394, 2016.

[27] P. Zrazhevskiy, S. R. Dave, and X. Gao, "Addressing key technical aspects of quantum dot probe preparation for bioassays," *Particle & Particle Systems Characterization*, vol. 31, no. 12, pp. 1291–1299, 2014.

[28] K. Susumu, E. Oh, J. B. Delehanty, J. B. Blanco-Canosa, B. J. Johnson, V. Jain, W. J. Hervey IV, W. R. Algar, K. Boeneman, P. E. Dawson et al., "Multifunctional compact zwitterionic ligands for preparing robust biocompatible semiconductor quantum dots and gold nanoparticles," *Journal of the American Chemical Society*, vol. 133, no. 24, pp. 9480–9496, 2011.

[29] E. L. Elson and D. Magde, "Fluorescence correlation spectroscopy. i. conceptual basis and theory," *Biopolymers*, vol. 13, no. 1, pp. 1–27, 1974.

[30] D. Magde, E. L. Elson, and W. W. Webb, "Fluorescence correlation spectroscopy. ii. an experimental realization," *Biopolymers*, vol. 13, no. 1, pp. 29–61, 1974.

[31] R. Rigler, Ü. Mets, J. Widengren, and P. Kask, "Fluorescence correlation spectroscopy with high count rate and low background: analysis of translational diffusion," *European Biophysics Journal*, vol. 22, no. 3, pp. 169–175, 1993.

[32] P. Schwille, "Fluorescence correlation spectroscopy and its potential for intracellular applications," *Cell biochemistry and biophysics*, vol. 34, no. 3, pp. 383–408, 2001.

[33] P.-O. Gendron, F. Avaltroni, and K. Wilkinson, "Diffusion coefficients of several rhodamine derivatives as determined by pulsed field gradient–nuclear magnetic resonance and fluorescence correlation spectroscopy," *Journal of fluorescence*, vol. 18, no. 6, pp. 1093–1101, 2008.

[34] G. U. Nienhaus, P. Maffre, and K. Nienhaus, "Studying the protein corona on nanoparticles by fcs," *Methods Enzymol*, vol. 519, pp. 115–37, 2012.

[35] S. Kalinin, R. Kühnemuth, H. Vardanyan, and C. A. M. Seidel, "Note: A 4 ns hardware photon correlator based on a general-purpose field-programmable gate array development board implemented in a compact setup for fluorescence correlation spectroscopy," 2012.

[36] *Absolute Diffusion Coefficients: Compilation of Reference Data for FCS Calibration*, PicoQuant.

[37] A. de Thomaz, D. Almeida, V. Pelegati, H. Carvalho, and C. Cesar, "Measurement of the hydrodynamic radius of quantum dots by fluorescence correlation spectroscopy excluding blinking," *The Journal of Physical Chemistry B*, vol. 119, no. 11, pp. 4294–4299, 2015.

[38] S. Doose, J. M. Tsay, F. Pinaud, and S. Weiss, "Comparison of photophysical and colloidal properties of biocompatible semiconductor nanocrystals using fluorescence correlation spectroscopy," *Analytical Chemistry*, vol. 77, no. 7, pp. 2235–2242, 2005.

[39] T. Liedl, S. Keller, F. C. Simmel, J. O. Rädler, and W. J. Parak, "Fluorescent nanocrystals as colloidal probes in complex fluids measured by fluorescence correlation spectroscopy," *Small*, vol. 1, no. 10, pp. 997–1003, 2005.

[40] P. Maffre, S. Brandholt, K. Nienhaus, L. Shang, W. J. Parak, and G. U. Nienhaus, "Effects of surface functionalization on the adsorption of human serum albumin onto nanoparticles–a fluorescence correlation spectroscopy study," *Beilstein journal of nanotechnology*, vol. 5, no. 1, pp. 2036–2047, 2014.

[41] G. W. Stroke, *Diffraction Gratings*. Berlin, Heidelberg: Springer Berlin Heidelberg, 1967, pp. 426–754. [Online]. Available: http://dx.doi.org/10.1007/978-3-642-46077-7_8

[42] M. Okano, Y. Hirai, and H. Kikuta, "Optimal design for nonperiodic fine grating structure controlled by proximity correction with electron-beam lithography," *Japanese Journal of Applied Physics, Part 1: Regular Papers and Short Notes and Review Papers*, vol. 46, no. 2, pp. 627–632, 2007.

[43] L. Assoufid, O. Hignette, M. Howells, S. Irick, H. Lammert, and P. Takacs, "Future metrology needs for synchrotron radiation grazing-incidence optics," in *Nuclear Instruments and Methods in Physics Research, Section A: Accelerators, Spectrometers, Detectors and Associated Equipment*, vol. 467-468, 2001, pp. 267–270.

[44] P. Z. Takacs, "Metrology of reflection optics for synchrotron radiation," *Nuclear Inst. and Methods in Physics Research, A*, vol. 246, no. 1-3, pp. 227–241, 1986.

[45] S. Qian, W. Jark, and P. Z. Takacs, "The penta-prism LTP: A long-trace-profiler with stationary optical head and moving penta prism," *Review of Scientific Instruments*, vol. 66, no. 3, pp. 2562–2569, 1995.

[46] S. Qian, H. Li, and P. Z. Takacs, "Penta-prism long trace profiler (ppltp) for measurement of grazing incidence space optics," pp. 108–114, 1996. [Online]. Available: http://dx.doi.org/10.1117/12.245083

[47] P. Z. Takacs, E. L. Church, C. J. Bresloff, and L. Assoufid, "Improvements in the Accuracy and the Repeatability of Long Trace Profiler Measurements," *Applied Optics*, vol. 38, no. 25, p. 5468, 1999. [Online]. Available: http://ao.osa.org/abstract.cfm?URI=ao-38-25-5468

[48] L. Assoufid, N. Brown, D. Crews, J. Sullivan, M. Erdmann, J. Qian, P. Jemian, V. V. Yashchuk, P. Z. Takacs, N. A. Artemiev, D. J. Merthe, W. R. McKinney, F. Siewert, and T. Zeschke, "Development of a high-performance gantry system for a new generation of optical slope measuring profilers," *Nuclear Instruments and Methods in Physics Research, Section A: Accelerators, Spectrometers, Detectors and Associated Equipment*, vol. 710, pp. 31–36, 2013.